A NON-DESTRUCTIVE TESTING METHOD ON CHARACTERIZING THE CURING PROCESS OF COATED MATERIALS WITH LINE-FOCUS SURFACE WAVE TRANSDUCER SYSTEM

by

Yuxiang Wang

Bachelor of Science, Nanjing University, 2015

Submitted to the Graduate Faculty of

Swanson School of Engineering in partial fulfillment

of the requirements for the degree of

Master of Science

University of Pittsburgh

2016

UNIVERSITY OF PITTSBURGH

SWANSON SCHOOL OF ENGINEERING

This thesis was presented

by

Yuxiang Wang

It was defended on

November 22, 2016

and approved by

Qingming Wang, Ph.D., Professor

Department of Mechanical Engineering and Materials Science

Jeffrey Vipperman, Ph.D., Professor

Department of Mechanical Engineering and Materials Science

Patrick Smolinski, Ph.D., Associate Professor,

Department of Mechanical Engineering and Materials Science

Thesis Advisor: Qingming Wang, Ph.D., Professor,

Department of Mechanical Engineering and Materials Science

A NON-DESTRUCTIVE TESTING METHOD ON CHARACTERIZING THE CURING PROCESS OF COATED MATERIALS WITH LINE-FOCUS SURFACE WAVE TRANSDUCER SYSTEM

Yuxiang Wang, M.S.

University of Pittsburgh, 2016

As part of the modern life, coating material is playing a silent but functional role in every aspect, especially among auto-mobile and medal manufacturing industry. However, the conventional coating process would typically end in a time consuming curing process that is relatively difficult to be characterized quantitatively. In this article, an efficient approach was brought upon to characterize the curing process of typical coated materials, using a line-focus transducer testing system to measure the properties of the surface wave of the coated sample.

A line focus ultrasonic testing system is established, which is completely non-invasive, timesaving, and highly automated owning to the control system written on LabView environment and a step motor platform. This research also provides some useful hint for the future reference on the operation standard of the similar testing platform.

This research mainly consists of 3 parts: 1) the brief theoretical introduction of the surface wave theorem and the establishment of the testing system. 2) the testing procedure on the coating

samples with related signal process, evaluating the surface wave speed and amplitude. 3) the conclusions of the experiments and future expectations from this testing platform.

TABLE OF CONTENTS

LIST OF TABLES

LIST OF FIGURES

NOMENCLATURE

c	Sound Speed
λ	Wave Length
ρ	Density
v	Particle Speed
n	Normal vector
z_0	Characteristic Impedance
Z_a	Acoustic Impedance
Z_s	Specific Acoustic Impedance
Z_n	Normal Specific Acoustic Impedance
j	Imaginary Unit
ω	Angular Velocity
σ	Poisson's Ratio
Φ	Velocity Potential
ψ	Vector Potential
θ	Critical Angle

ACKNOWLEDGEMENT

I would love to present my sincere gratitude to all the kind people who supported me throughout this research project.

Firstly I would like to thank my advisor Prof. Qing-Ming Wang, for all his patience and guidance during my master period. There's no way that I could reach this far without his assist. Also I sincerely appreciate my committee members, Dr. Jeff Vipperman and Dr. Patrick Smolinski, for their advice on making this thesis better. Furthermore, the support and understanding from my future PhD advisor Dr. Chris Brown is also appreciated.

Secondly, my thanks to my research group members Qiuyan Li, Hongfei Zu, Huiyan Wu and Xuande Zhang, their knowledge and experience has been a great help. Special thanks to Xiao Ma who enlightened me on the signal processing.

In addition, my gratitude to my dear girlfriend Muying, for her support and love throughout this year.

Finally, I would like to present this thesis for my beloved parents.

1.0 INTRODUCTION

In this research, we intended to evaluate the curing process of the coating materials in auto industry, by measuring the properties of the surface wave collected from the coated samples. The ultimate goal of the research is the real time evaluation of the curing of the auto coating.

We choose to build a line-focus ultrasonic transducer to do all the measurements related, and the theoretical basis for the acoustic measurement as well as the transducer system is presented in the following sections in this chapter.

In Chapter 2, the details of the hardware and software programming of this system is presented.

In Chapter 3, the testing protocols including the making of the sample and the detailed test procedure is brought up.

Chapter 4 shows the data processing procedure of the data collected in each experiments, as well as the results for the surface wave velocity and intensity transmission factor calculated for the samples.

Chapter 5 presents the extended applications for the test system.

Conclusions and future work will be drawn in Chapter 6.

1.1 ULTRASONIC TESTING FUNDAMENTALS

1.1.1 Acoustic governing equation.

In fluid, the governing equations for linear vibration is given by [1]:

$\rho_0 \frac{\partial^2 \mathbf{v}}{\partial x^2} = -\boldsymbol{\nabla} p$ Equation of Motion

$\frac{\partial \rho'}{\partial t} + \rho_0 \boldsymbol{\nabla} \cdot \mathbf{v} = 0$ Equation of Continuity

$p = {c_0}^2 \rho'$ Equation of State

where $\boldsymbol{\nabla}$ is the gradient operator, ρ_0 is the static density.

By combining these equations, the linear vibration equation could be derived as:

$$\frac{\partial^2 p}{\partial t^2} - {c_0}^2 \boldsymbol{\nabla^2} p = 0$$

where $\boldsymbol{\nabla^2} = \frac{\partial^2}{\partial x^2} + \frac{\partial^2}{\partial y^2} + \frac{\partial^2}{\partial z^2}$ in rectangular coordinate system.

For a irrotational situation, consider $\boldsymbol{\nabla} \times \mathbf{v} = 0$, let $\mathbf{v} = -\boldsymbol{\nabla}\Phi$, we have

$$\frac{\partial^2 \Phi}{\partial t^2} - {c_0}^2 \boldsymbol{\nabla^2} \Phi = 0$$

and Φ is the velocity potential.

From the equation of state we can derive that

$$\Phi = \int \frac{p}{\rho_0} dt$$

hence,

$$p = \rho_0 \frac{\partial \Phi}{\partial t}$$

In this case, as long as Φ is known, we can calculate both particle speed **v** and sound pressure p. For a plane acoustic wave in fluid, we have:

$p = p(c_0 t - \mathbf{n} \cdot \mathbf{x})$ for the pressure wave

$\mathbf{v} = -\frac{1}{\rho_0} \int \nabla p \, dt = \frac{p}{\rho_0 c_0} \mathbf{n}$ for the speed wave

where $\rho_0 c_0$ is the characteristic impedance, z_0.

1.1.2 Acoustic wave propagation through interface.

For a harmonic plane acoustic wave in a medium, the solution to the governing equation can be written in the form of:

$$p = p_a e^{j(\omega t \mp kx)}, \ \ (k = \frac{\omega}{c_0})$$

Alongside the path of the propagation, if the travelling wave reaches the medium with different acoustical property (characteristic impedance z_0), it would lead to reflection, transmission and refraction. The figure below describes the waveform at the interface, where $\boldsymbol{p_i}$, $\boldsymbol{p_t}$ and $\boldsymbol{p_r}$ stands for incident, transmit and reflected wave sound pressure.

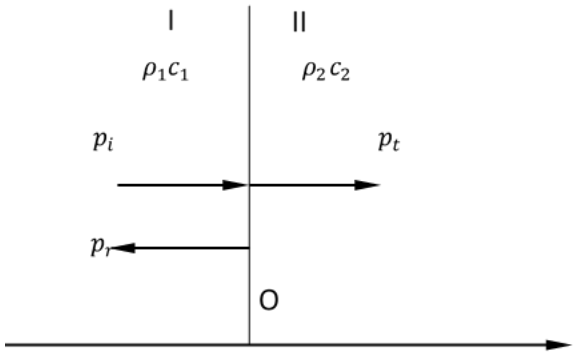

Figure 1. Acoustic wave propagation through the interface

At the interface, the acoustic boundary condition should be considered. Define the normal specific acoustic impedance at the interface,

$$Z_n = \frac{p}{\mathbf{v} \cdot \mathbf{n}}$$

For the boundary condition,

$p_1 = p_2$ sound pressure continuity

$\mathbf{v_1} \cdot \mathbf{n} = \mathbf{v_2} \cdot \mathbf{n}$ normal velocity continuity

we then have the equal normal specific acoustic impedance at the interface:

$$Z_{n1} = Z_{n2}$$

thus

$$\begin{cases} p_i + p_r = p_t \\ v_i + v_r = v_t \end{cases}$$

and the reflection/transmission factor for sound pressure and velocity are:

$$\begin{cases} r_p = \dfrac{p_r}{p_i} = \dfrac{R_{12} - 1}{R_{12} + 1} \\ r_v = \dfrac{v_r}{v_i} = \dfrac{1 - R_{12}}{1 + R_{12}} \\ t_p = \dfrac{p_t}{p_i} = \dfrac{2R_{12}}{1 + R_{12}} \\ t_v = \dfrac{v_t}{v_i} = \dfrac{2}{1 + R_{12}} \end{cases}$$

where $R_{12} = \frac{\rho_2 c_2}{\rho_1 c_1}$, $R_{21} = \frac{\rho_1 c_1}{\rho_2 c_2}$

In addition, for the reflection/transmission factor of the sound intensity,

$$\begin{cases} r_I = \dfrac{I_r}{I_i} = \left(\dfrac{R_{12} - 1}{R_{12} + 1}\right)^2 \\ t_I = \dfrac{I_t}{I_i} = \dfrac{4R_{12}}{(1 + R_{12})^2} \end{cases}$$

For an even more complicated situation, when the acoustic wave is propagating through three different medium, in other words, an interlayer:

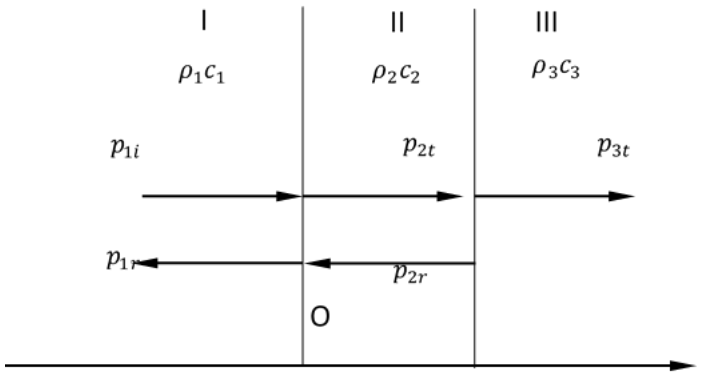

Figure 2. Acoustic wave propagation through double interface

After adapting the acoustic boundary condition, the transmission factor for the sound intensity could be derived as:

$$t_I = \frac{I_t}{I_i} = \frac{4R_1R_3}{(R_1+R_3)^2\cos^2 k_2D + (R_2 + \frac{R_1R_3}{R_2})^2 \sin^2 k_2D}$$

where R stands for the characteristic impedance of the corresponding medium, and D for the thickness of the interlayer.

1.1.3 Acoustic wave oblique incidence through interface

Consider the oblique incidence of the travelling wave at the surface of two different media, reflection and refraction would occur.

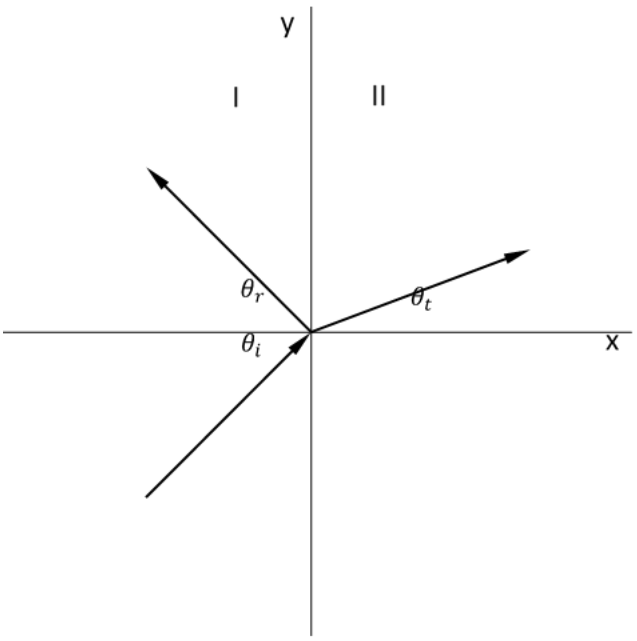

Figure 3. Acoustic waveform of oblique incidence at interface

Again, by applying sound pressure and normal velocity continuity,

$$\begin{cases} p_i + p_r = p_t \\ v_{ix} + v_{rx} = v_{tx} \end{cases}$$

using the previous definition,

$$\begin{cases} p_{ia}e^{-jk_1 y \sin\theta_i} + p_{ra}e^{-jk_1 y \sin\theta_r} = p_{ta}e^{-jk_2 y \sin\theta_t} \\ \dfrac{\cos\theta_i}{\rho_1 c_1} p_{ia}e^{-jk_1 y \sin\theta_i} - \dfrac{\cos\theta_r}{\rho_1 c_1} p_{ra}e^{-jk_1 y \sin\theta_r} = \dfrac{\cos\theta_t}{\rho_2 c_2} p_{ta}e^{-jk_2 y \sin\theta_t} \end{cases}$$

where $k_1 = \frac{\omega}{c_1}, k_2 = \frac{\omega}{c_2}$

To satisfy every y location on the interface, the exponential factor must be same:

$$k_1 \sin\theta_i = k_1 \sin\theta_r = k_2 \sin\theta_t$$

thus,

$$\begin{cases} \theta_i = \theta_r \\ \dfrac{\sin\theta_i}{\sin\theta_t} = \dfrac{k_2}{k_1} = \dfrac{c_1}{c_2} \end{cases}$$

Such is the Snell law for fraction.

1.1.4 Acoustic wave in solid material

In the case for elastic solid, the governing acoustic equation could be derived from the stress element [2].

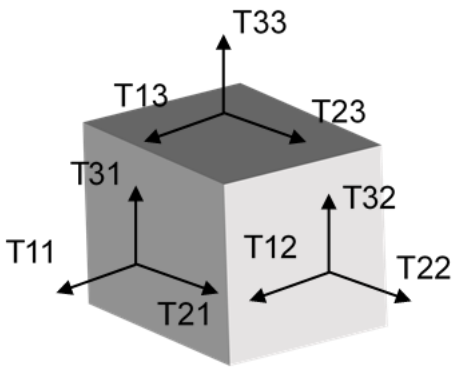

Figure 4. Stresses on a differential mechanical element

For elastic, isotropic medium, the stress are linked to strains by:

$$\begin{bmatrix} T_1 \\ T_2 \\ T_3 \\ T_4 \\ T_5 \\ T_6 \end{bmatrix} = \begin{bmatrix} \lambda+2\mu & \lambda & \lambda & 0 & 0 & 0 \\ \lambda & \lambda+2\mu & \lambda & 0 & 0 & 0 \\ \lambda & \lambda & \lambda+2\mu & 0 & 0 & 0 \\ 0 & 0 & 0 & \mu & 0 & 0 \\ 0 & 0 & 0 & 0 & \mu & 0 \\ 0 & 0 & 0 & 0 & 0 & \mu \end{bmatrix} \begin{bmatrix} S_1 \\ S_2 \\ S_3 \\ S_4 \\ S_5 \\ S_6 \end{bmatrix}$$

where

$$T_{11} = T_1 \qquad T_{23} = T_{32} = T_4$$

$$T_{22} = T_2 \qquad T_{13} = T_{31} = T_5$$

$$T_{33} = T_3 \qquad T_{12} = T_{21} = T_6$$

λ and μ are the first and second Lame constant, and for fluids, $\mu = 0$, as it stands for the shear mode for material vibration.

Similarly, the equation of motion could be derived as (first considering the motion in 1 dimension, e.g. x_3 direction):

$$\frac{\partial T_3}{\partial x_3} + \frac{\partial T_4}{\partial x_2} + \frac{\partial T_5}{\partial x_1} = \rho \frac{\partial^2 \mathrm{v}_3}{\partial t^2}$$

for plane longitudinal wave case where no shear stress involved, the equation is reduced to

$$T_3 = (\lambda + 2\mu) S_3 = (\lambda + 2\mu) \frac{\partial \mathrm{v}_3}{\partial x_3}$$

and

$$\frac{\partial T_3}{\partial x_3} = \rho \frac{\partial^2 \mathrm{v}_3}{\partial t^2}$$

as T_3 now stands for the opposite of the acoustic pressure, p. Simplifying it:

$$\frac{\partial^2 \mathrm{v}_3}{\partial {x_3}^2} = \frac{\rho}{\lambda + 2\mu} \frac{\partial^2 \mathrm{v}_3}{\partial t^2}$$

And consider the 3 dimension case, let the velocity field

$$\mathbf{v} = \boldsymbol{\nabla}\phi + \boldsymbol{\nabla} \times \psi$$

where ϕ is scalar potential and ψ is vector potential. Then we have two separate equation (the curl of a scalar is zero):

$$\begin{cases} \rho \dfrac{\partial^2 \Phi}{\partial t^2} = (\lambda + 2\mu) \boldsymbol{\nabla^2} \Phi \\ \rho \dfrac{\partial^2 \psi}{\partial t^2} = \mu \boldsymbol{\nabla^2} \psi \end{cases}$$

in the two cases, we let

$$\begin{cases} c_L = \sqrt{\dfrac{\lambda + 2\mu}{\rho}} \\ c_T = \sqrt{\dfrac{\mu}{\rho}} \end{cases}$$

as the speed of the longitudinal(Primary) and transverse(Shear) wave mode. Both the P-wave and S-waves are categorized as bulk waves because they represent disturbances propagating in the bulk or elastic solid.

In addition, the relation of Young's module (E) and Poisson's Ratio (σ) to Lame constant λ, μ are

$$\begin{cases} \lambda = \dfrac{E\sigma}{(1+\sigma)(1-2\sigma)} \\ \mu = \dfrac{E}{2(1+\sigma)} \end{cases}$$

1.1.5 Surface wave theorem

In addition to bulk waves, a number of other wave types also exist in solid material, such as surface (Rayleigh) wave, normal (Lamb) wave, and several other types of guided waves.

In 1885, the English scientist Lord Rayleigh demonstrated theoretically that waves can be propagated along the plane boundary between an elastic half-space and a vacuum or sufficiently rarefied medium (i.e. air), and the amplitude of the waves decays rapidly with depth.

A surface wave combines longitudinal and vertically polarized shear waves travelling the surface of a relatively thick solid material, penetrating to a depth of one wavelength. Therefore Surface wave combines both a longitudinal and transvers motion to create an elliptic orbit motion as shown in the image below [3].

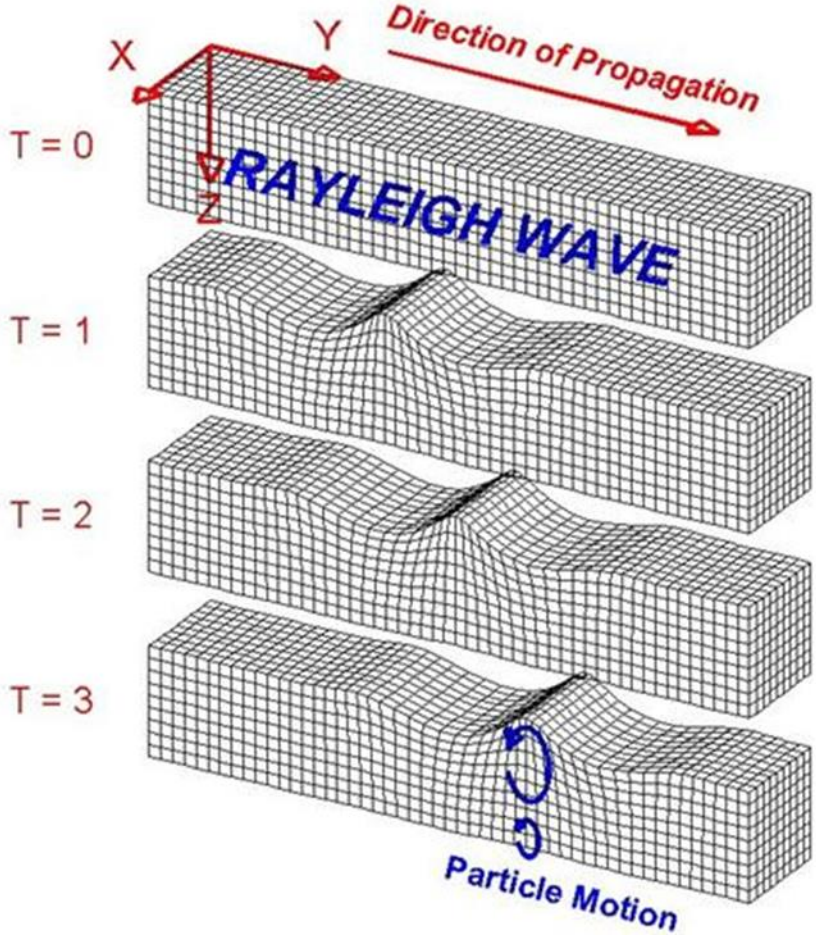

Figure 5. A Rayleigh Wave Travels through a Medium

The governing equation for the surface could be derived as :

$$\begin{cases} \phi = \phi_a e^{-\alpha x} e^{j(\omega t - k_s x)} \\ \psi = \psi_a e^{-\beta x} e^{j(\omega t - k_s x)} \end{cases}$$

From the motion equation, we can derive:

$$\begin{cases} a^2 = {k_s}^2 - {k_L}^2 \\ \beta^2 = {k_s}^2 - {k_T}^2 \end{cases}$$

where $k_s = \frac{\omega}{c_s}$ is the wave number for the surface wave c_s

The relation between surface wave c_s and transverse wave c_T can be derived as:

$$\left[1-2(\frac{{c_T}^2}{{c_s}^2})^2\right]\left(\beta^2+\frac{\omega^2}{{c_s}^2}\right)+4\alpha\beta\left(\frac{c_T}{c_s}\right)^2=0$$

for Poisson's ratio varying 0~0.5, $\frac{c_T}{c_s}$ value varies from 0.814~0.55

In the cases of this research, the reflected wave are the combination of various types of both bulk waves and surface waves.

1.1.6 Piezoelectric effect

Piezoelectricity was first discovered by Pierre Curie and Paul Jacques in 1880, referring to generating an electric charge in a material when subjecting it to applied stress, and conversely, generating a mechanical strain in response to an applied electrical field. In some dielectric materials (crystals, ceramics, polymers) without center symmetry, an electric polarization can be generated by the application of mechanical stresses, such is called piezoelectricity [4]:

$$P = d\,\sigma \qquad \text{Direct effect}$$

$$\varepsilon = d\,E \qquad \text{Converse effect}$$

where P stands for polarization,

σ stands for stress,

ε stands for strain

d stands for piezoelectric coefficient

in 3-dimension expression, we have:

$$\begin{bmatrix}P_1\\P_2\\P_3\end{bmatrix}=\begin{bmatrix}d_{11}&d_{12}&d_{13}&d_{14}&d_{15}&d_{16}\\d_{21}&d_{22}&d_{23}&d_{24}&d_{25}&d_{26}\\d_{31}&d_{32}&d_{33}&d_{34}&d_{35}&d_{36}\end{bmatrix}\begin{bmatrix}\sigma_1\\\sigma_2\\\sigma_3\\\sigma_4\\\sigma_5\\\sigma_6\end{bmatrix}$$

$$\begin{bmatrix}\sigma_1\\ \sigma_2\\ \sigma_3\\ \sigma_4\\ \sigma_5\\ \sigma_6\end{bmatrix} = \begin{bmatrix}d_{11} & d_{21} & d_{31}\\ d_{12} & d_{22} & d_{32}\\ d_{13} & d_{23} & d_{33}\\ d_{14} & d_{24} & d_{34}\\ d_{15} & d_{25} & d_{35}\\ d_{16} & d_{26} & d_{36}\end{bmatrix}\begin{bmatrix}P_1\\ P_2\\ P_3\end{bmatrix}$$

Below are the properties of some piezoelectric materials.

Table 1. Piezoelectric properties for some piezoelectric materials

Property	PZT ceramic	PVDF	ZnO film
d_{33}	220	-33	12
d_{31}	-93	23	-4.7
d_{15}	694		-12
k_{31}	0.31	0.12	
$tan\delta$	0.004	0.02	
Q	400		
ρc	30	2.7	

Piezoelectric strain coefficient	d
Electromechanical coupling	k_{33}, k_{31}, k_T
Dielectric constant	K
Dielectric loss tangent	$tan\delta$
Mechanical quality factor	Q
Acoustic impedance	ρc

1.1.7 PVDF material

PVDF is a fluoropolymer whose piezoelectricity was discovered by Heiji Kawai in 1969 [5], and has since become established as one of the most commonly used materials in acoustic imaging

devices. Commercially available PVDF also has a substantially lower cost than piezoelectric ceramics, and implementation involves relatively simple fabrication steps.

In the case of this research, the PVDF material work on the thickness mode, as a line focus transducer probe.

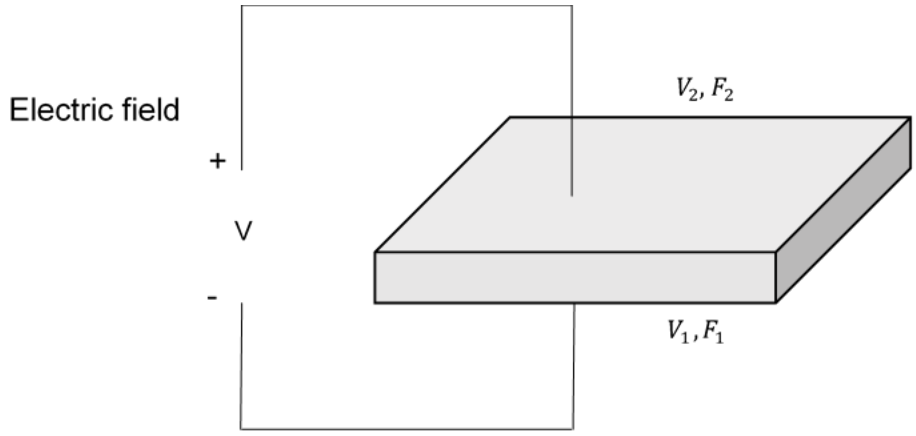

Figure 6. PVDF vibration mode

In this research, the designing of the PVDF line focus transducer design refers to the work of D. Xiang et.al, which is shown as follows [6].

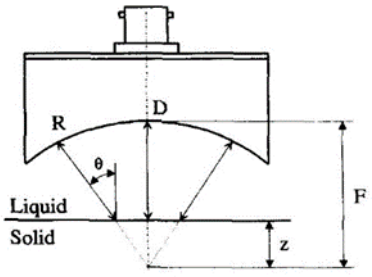

Figure 7. The transducer probe design adapted from D. Xiang et.al **[6]**

The PVDF thin film was fixed onto the cylindrical convex surface, and the interior is filled with high impedance metal material, tungsten power mixed with epoxy, for example, as backing material. The sample is placed within the focus radius, F, beneath the probe, where the surface acoustic wave is activated at curtain angle.

From the research of Koichiro et.al, a more detailed model analyses of wave propagation of a similar probe was proposed, where they use aluminum as sample [7].

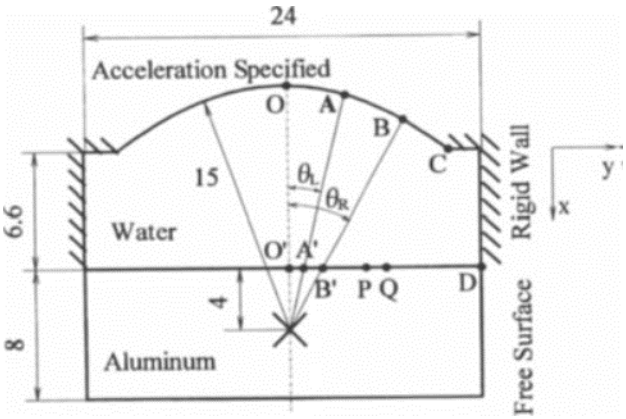

Figure 8. The 2 dimension acoustic field model adapted from Koichiro et.al **[7]**

After the stimulus is activated on the convex surface O-C, the wave propagated along the path BB' reaches the aluminum surface and the leaky Rayleigh wave with large amplitude is excited. Similarly, a while later the creeping wave (leaky longitudinal wave) is excited on the aluminum surface by the wave traveled along AA'.

Then the combined wave along the symmetric axis hits the point O' and the bulk waves propagate through the aluminum, which could be isolated from the time domain.

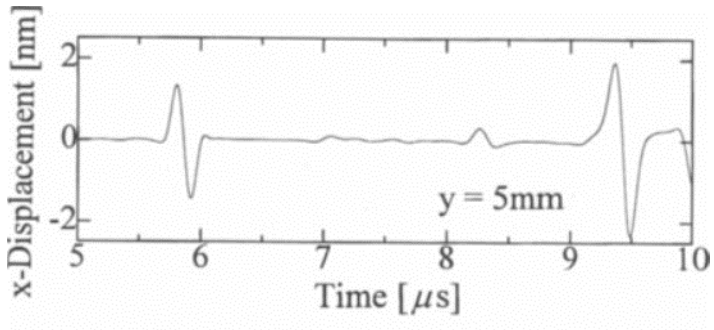

Figure 9. The calculated waveform from the model, adapted from Koichiro et.al **[7]**

The peaks are direct excitation, creeping wave and leaky Rayleigh wave, respectively. In actual experiments, creeping waves are barely observed:

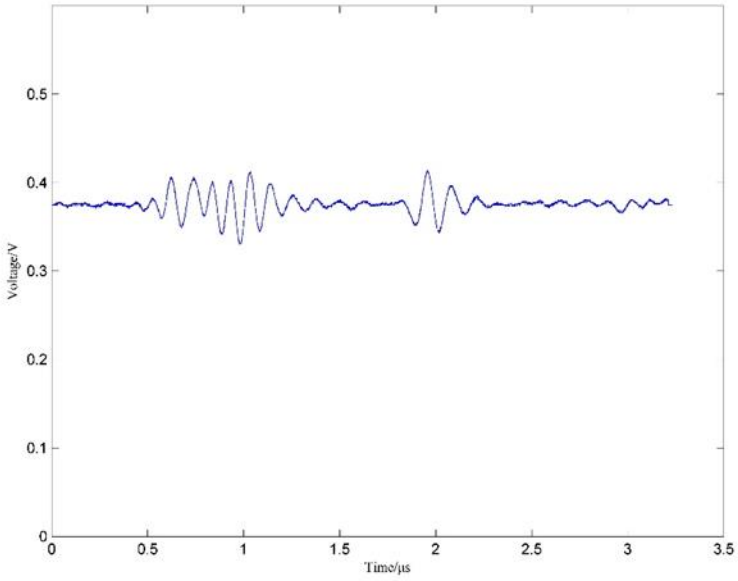

Figure 10. Actual surface waveform result from the test

From the figure of the probe in the research from D. Xiang et.al, the relation between the arrival time delay and the surface wave velocity can then be derived. If using the direct reflected wave as the reference, the arrival time for the leaky surface wave could be presented as:

$$t = \frac{2(1-\cos\theta)}{c_{Water}} z$$

where z is the defocus length between the surface of the sample and the focal point of the convex surface. c_{Water} is the sound speed in water as we use water as the coupling material in this research. Then we have:

$$\frac{dz}{dt} = \frac{c_{Water}}{2(1-\cos\theta)}$$

For θ as the critical angle of the surface wave,

$$\theta = \sin^{-1}(\frac{c_{Water}}{c_R})$$

where c_R is the speed of the surface wave for the sample.

In this way, we obtain the relation between the surface wave velocity, c_R and the slope of distance z as a function of the time delay t, $\frac{dz}{dt}$:

$$c_R = \left[\frac{1}{c_{Water}(\frac{dz}{dt})} - \frac{1}{4(\frac{dz}{dt})^2}\right]^{-1/2}$$

1.2 SECOND SECTION

1.2.1 Layers of typical coating

Vehicle paint systems are a combination of a clear coat (referred as protective barrier coat) and pigmented color coat (referred as base coat).

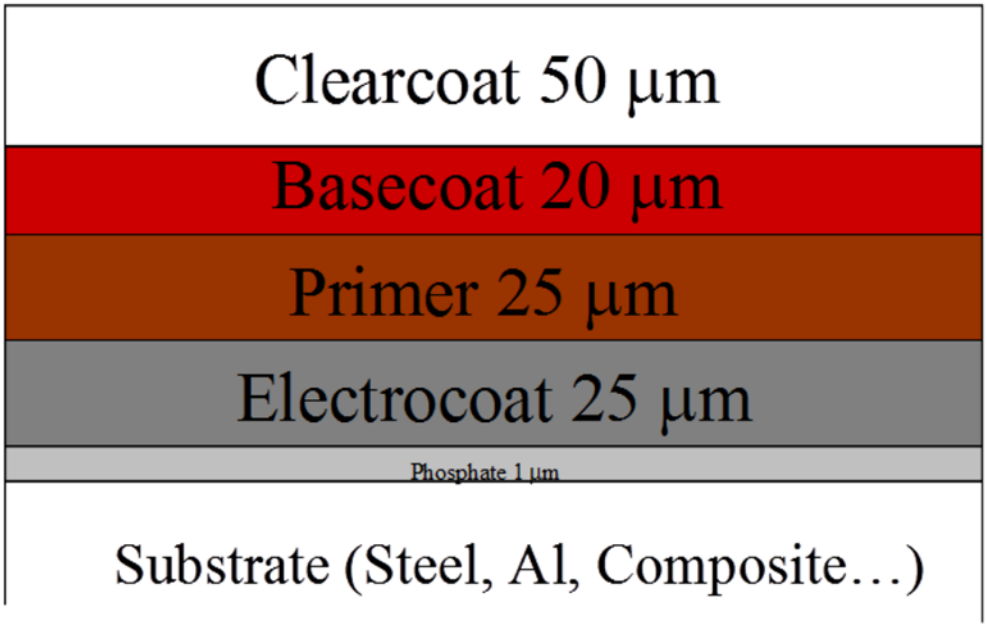

Figure 11. Typical auto coating layers(adapted from **http://www.mdpi.com/**)

For a steel plate to be coated, the first step is to apply the Electrocoat. The Electro-coating process is best described as a cross between plating and painting. It is a process where a metal part is immersed in a water-based solution containing a paint emulsion. An electric voltage is applied to the part causing the paint emulsion to condense onto the part

The second layer is called primer, which is used to increase adhesion for the next layer, also smoothening the surface of the electrocoat layer and providing limited protection from UV light.

The layer next to primer is called Basecoat, which contains the visual properties of color and effects. Base coat used in the automotive applications is commonly divided into three categories, solid, metallic, pearlescent colors.

The last layer which faces direct exposure to outer environment, is called Clearcoat. This final layer promotes glossiness of the surface, and also functions as the hardened protection for the

entire coating. In fact, clearcoat is the thickest layer of all the coating layers, takes half of the coating thickness.

Generally, the clear coat about 50 micron thick, which takes up most of the thickness in the coating layer. Whereas the pigmented color coat (base coat) is much thinner at 20 micron, and that is for the typical cars paints for today.

1.2.2 Curing process

The assembly line for the modern auto coating process consists of several coating and baking procedure in a certain sequence, which is so-called 3C1B or 3C2B processing.

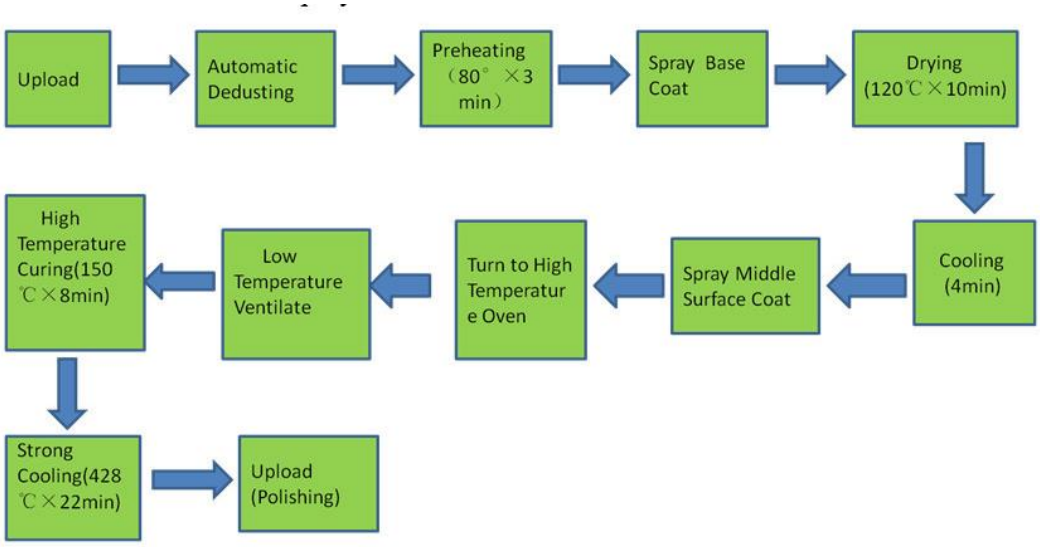

Figure 12. A typical production line for the auto coating

A three-coat one-bake (3C1B) type coating process is a typical practice for high efficiency and brings about an excellent finished appearance. After spraying all the three layers of paint, the

coated part was treated in high temperature oven for the coating to cure. For the 3C2B procedure, there's simply one more baking process immediately after the primer is sprayed.

1.2.3 Problems facing: evaluation of curing process

Noticed from the descriptions above, the curing process takes the most of the time during the entire coating line. And the evaluate the curing process, the traditional approach.

Traditional approach: CALORIMETRY

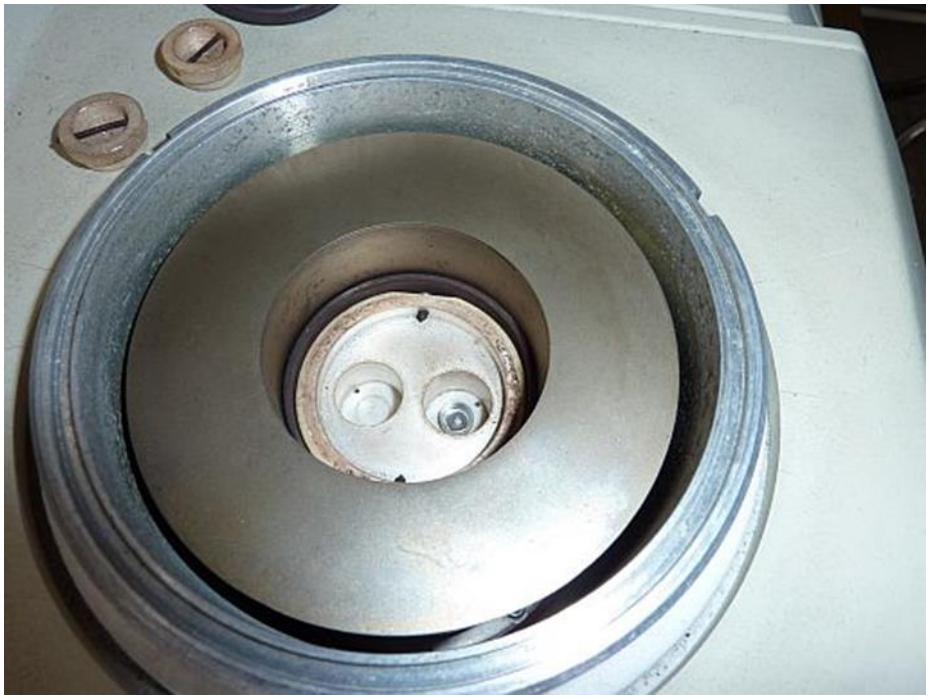

Figure 13. Inside of differential scanning calorimetry(DSC)

And this research is intended to use the line focus transducer testing system to evaluate the curing process of the coat, by evaluating the acoustic properties of the coated material as a whole, using a line-focus transducer testing system.

2.0 LINE-FOCUS ULTRASONIC TRANSDUCER SYSTEM BUILD UP

2.1 HARDWARE USED IN THE SYSTEM

Above is the schematic diagram of the Line-Focus Ultrasonic Testing System we built for testing the samples. The test system mainly consists of a motorized stage, a pulser/receiver, an oscilloscope with data acquisition function, and a PC that controls the devices all above.

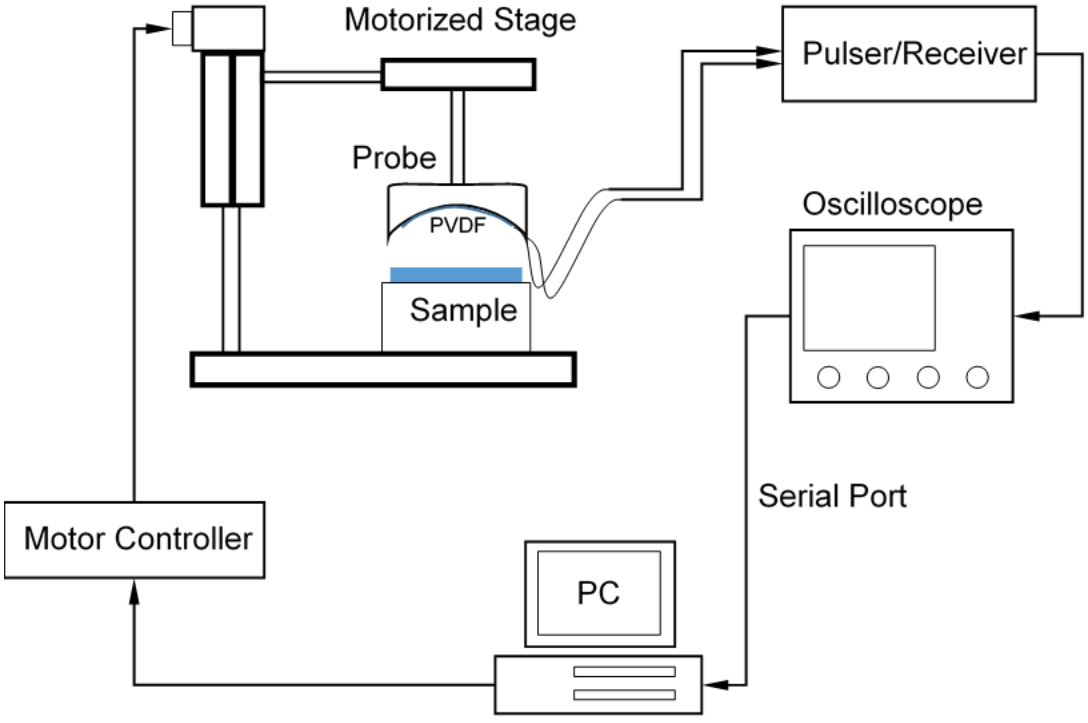

Figure 14. General layout of the testing system

The motorized stage is controlled by a motor controller linked by PC, with two axis control channels available. The travel range of the stage is +/- 10mm, with the maximum accuracy of 0.1μm.

The line-focus PVDF probe is mounted on the stage, and the pulser/receiver generates the impulse signal to the PVDF transducer, then receives the output signal from the transducer at the same time.

The output signal is sent to the oscilloscope controlled by PC, and the scope records each signal and sends the gathered data to PC through a serial port, as the motor stage varies probe position in different vertical direction.

An integrated control panel is written on the PC, controlling all the devices in the system.

2.2 LABVIEW PROGRAMMING ENVIRONMENT

Labview is chosen is be the programming environment for the control panel. Laboratory Virtual Instrument Engineering Workbench (LabVIEW) is a system-design platform and development environment for a visual programming language from National Instruments.

The programming language used in LabVIEW is a dataflow program language. Execution is determined by the structure of a graphical block diagram on which different functioning nodes are connected by drawing wires. This feature provides the multi-processing automatically by the built-in scheduler, which is one of the key feature that is required by the control program.

Labview also supports multiple types of devices, includes extensive support for interfacing to devices, instruments, cameras, and other devices. Users interface to hardware by either writing direct bus commands (USB, GPIB, Serial) or using device specific drivers that provide native LabVIEW function nodes for controlling the device, which is also important in this system.

2.3 PROGRAMMING FOR THE MOTOR

The model of the motorized stage we chose is KZC06020-C from SURUGA SEIKI, where some key parameters are listed below.

Table 2. Key parameters of the motor stage

Travel distance[mm]	20
Size of stage face[mm]	[square]60
Feed screw[Ball screw]	phi 8 lead 1
Material	Aluminum
Weight[kg]	0.8
Resolution(pulse)micro step	2micrometer/1micrometer
Resolution(pulse)micro step	0.1micrometer(1/20)
MAXspeed[mm/sec]	20
Load capacity(excited)	5.0kg

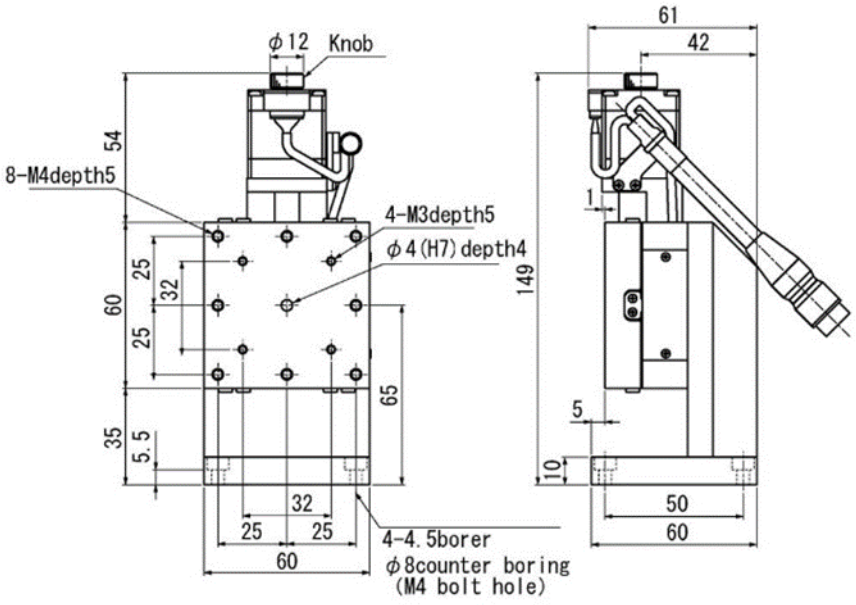

Figure 15. Front and side view of the motorized stage (adapted from **http://eng.surugaseiki.com/**)

The motorized stage is controlled by a DS102 stepping motor controller, which generates the control impulse to the motor, and is linked to PC by USB port. There are two channels available for the controller, and the channels are functioning independently.

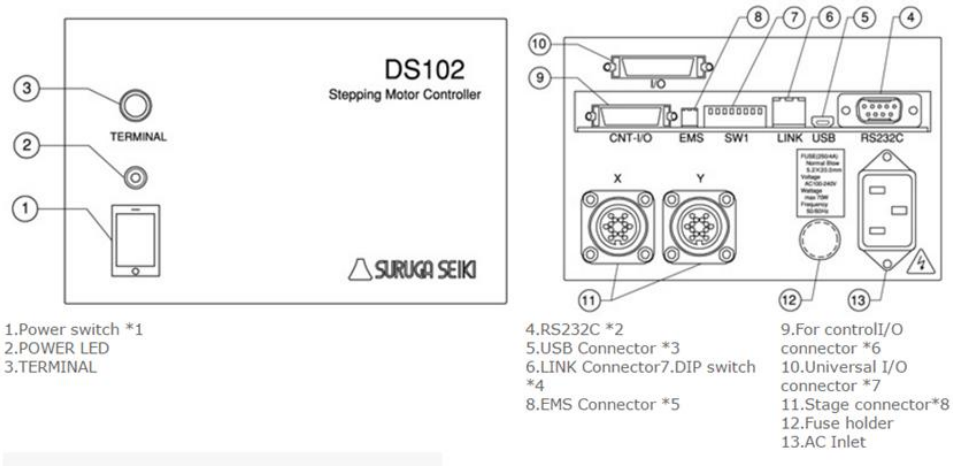

Figure 16. Front and rear panels of the controller (adapted from **http://eng.surugaseiki.com/**)

To control the motor stage, the Serial Communication programming in Labview is required.

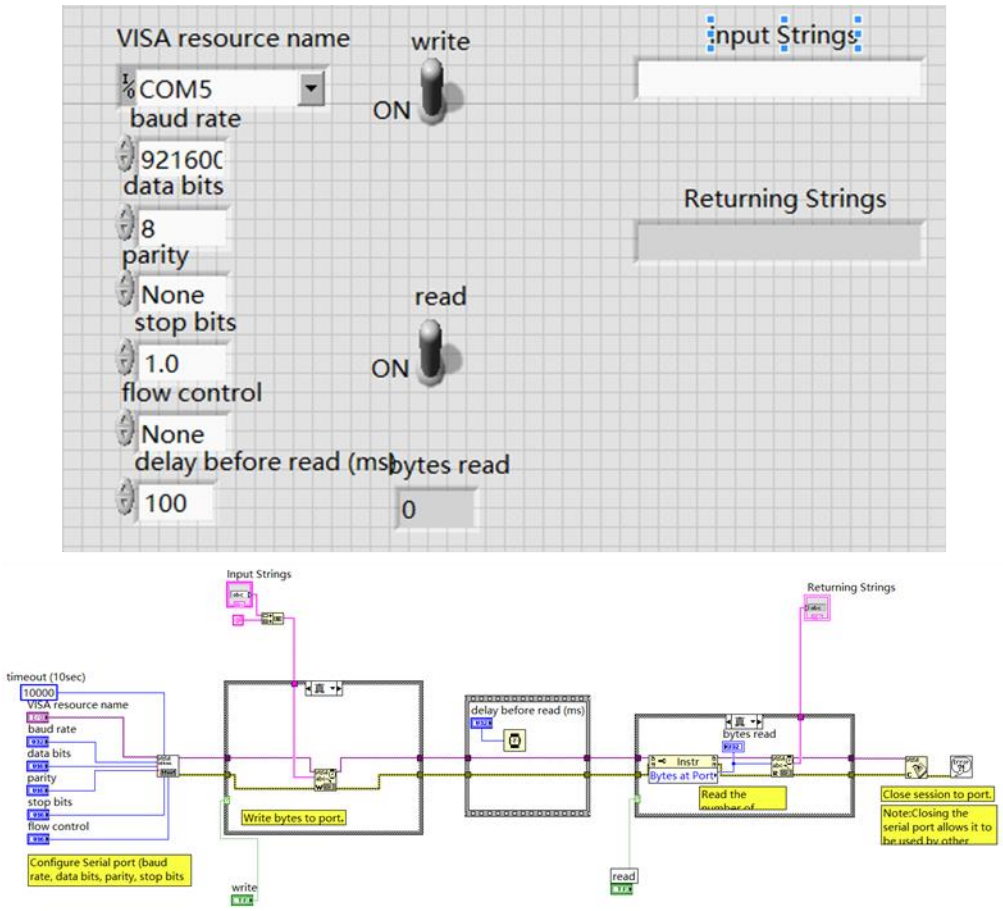

Figure 17. Front panel and block diagram of the serial communication VI

Using it as a sub-VI, the only thing we need to do is to use the command strings provided by the manufacturer as the input string to send to the controller. Various command statements could be found on the user manual, including Ready Check, Setting Initial Acceleration, Setting Speed, Travel Absolute and Relative Distance, Position Detection, etc.

By calling the sub VI with different commands, a motor control VI is written, with full function of setting speed table(the manufacturer provides 9 speed tables), travelling to designated position, and showing the real time position of the motor travel.

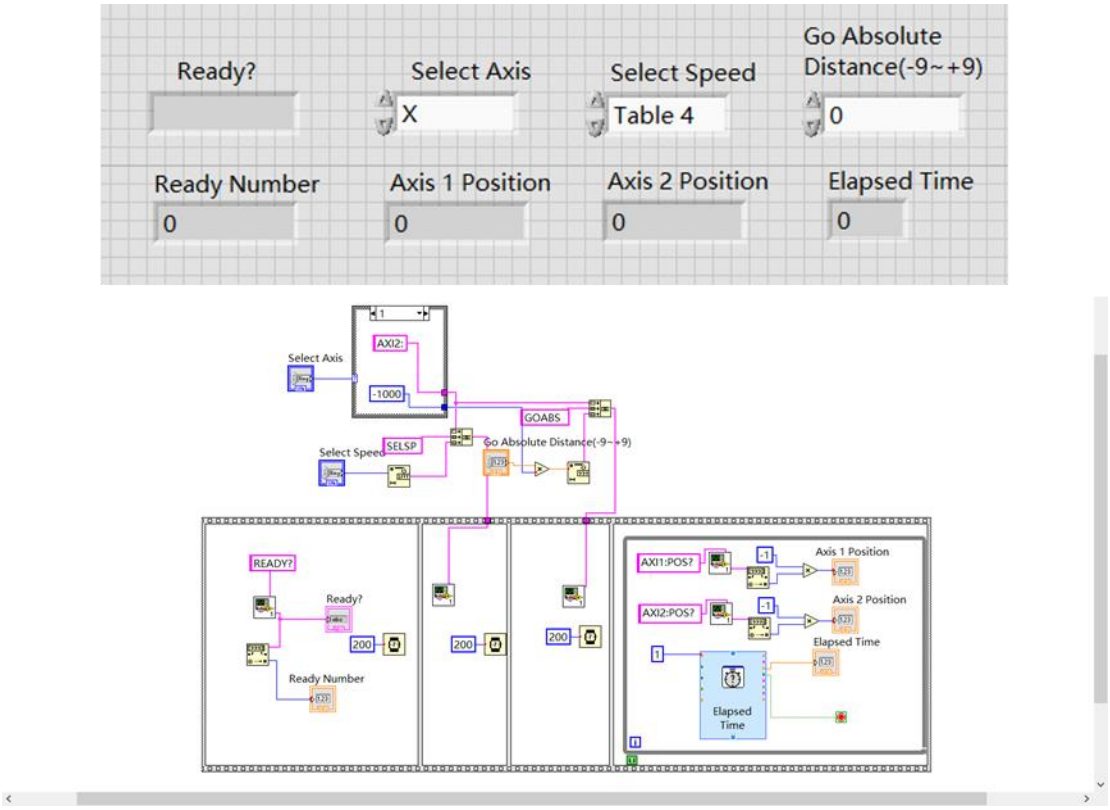

Figure 18. Front panel and block diagram of the motor control full VI

In time sequence, after executing the VI, a command is sent first to confirm that the controller is ready for later input, then wait for 200ms. Then the selected speed table and the designated position are send to the controller with 200ms delay also.

The controller drives the motor to move immediately when the Travel command is executed, and at the meantime, a Position Inquiry command is executed continuously, returning the real time position of the motor as it travels to the designated position.

This motor control VI is highly reliable without one single failure, and is used as a sub VI for the later control program of the whole system.

2.4 PROGRAMMING FOR THE OSCILLOSCOPE

The control of the oscilloscope is the key to the whole testing system, as we prefer the data collected to be as detailed as possible, and the process of data saving to be as timely as possible. In order to accomplish that, an auto-scaling and auto-saving Labview program becomes necessary.

The model of the oscilloscope being used in the system is Agilent DSO-X 4024A, with 200Mhz frequency span and up to 1,000,000 wfms/s update rate. An usb B type port is provided for external communication, which allows us to compile and perform data acquisition on Labview through PC. Although high speed port (like PCIe) is not supported on 4024A, it's still possible to collect data line through line with usb port through serial communication VI.

Figure 19. Front panel and rear panel of DSO-X 4024A oscilloscope

National Instruments provided a sample VI for the basic controlling of the oscilloscope, featuring in a single waveform acquisition. Similar to the motor control program, this VI also uses serial port communication for the control, and in the block diagram of the sample VI, the detailed command strings are provided for advanced operation on the oscilloscope.

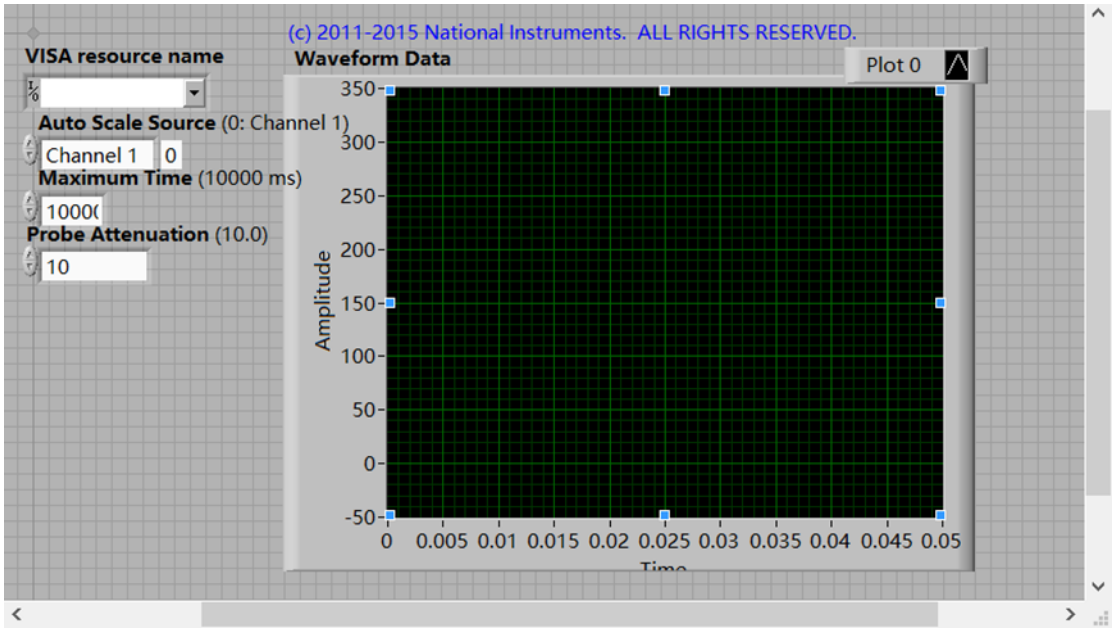

Figure 20. Front panel of the sample data collecting VI from NI

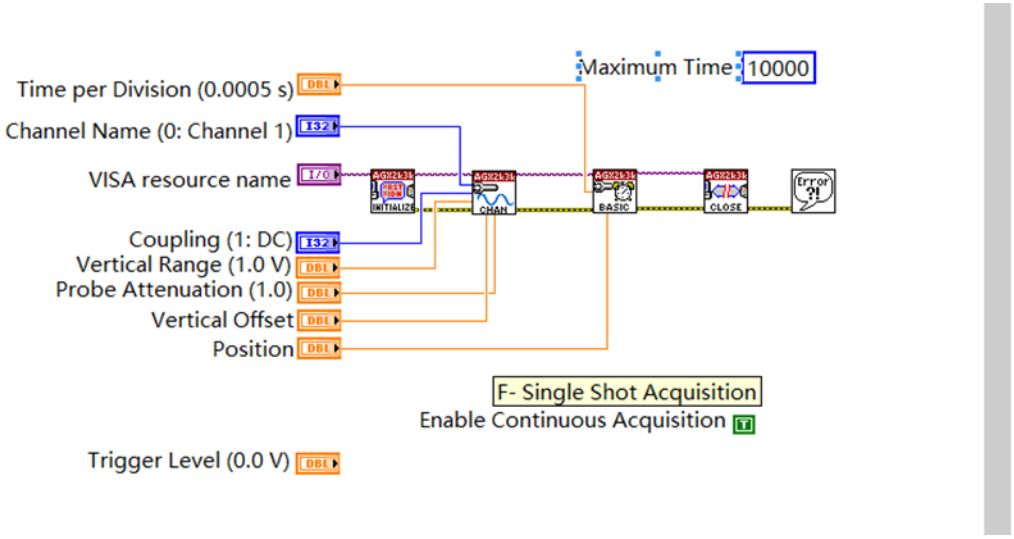

Figure 21. Detailed command for controlling various parameters of the oscilloscope

By adapting those command strings, a fully function data acquisition VI is developed, featuring in recording the displayed data in full, with any assigned horizontal span.

For the kernel VI that is functioning in data recording, a file write/read function is added.

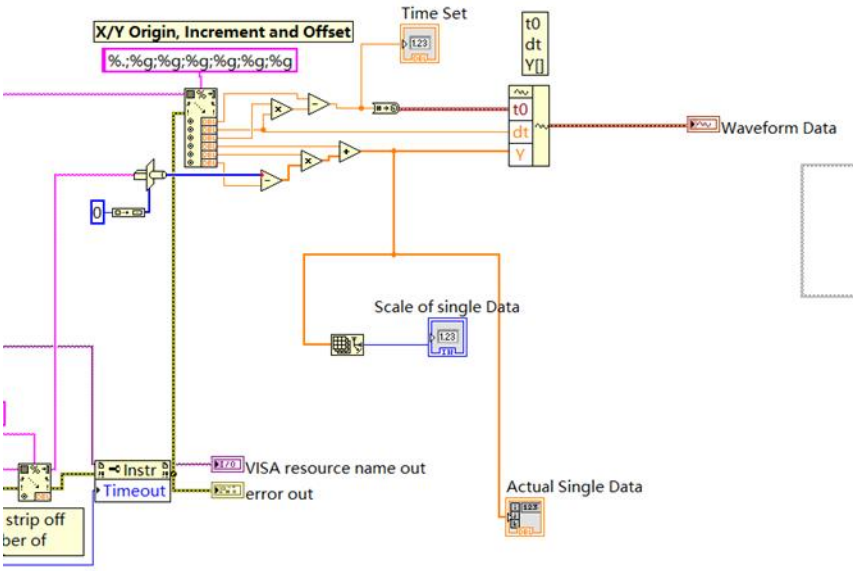

Figure 22. Adding file w/r function in waveform saving VI

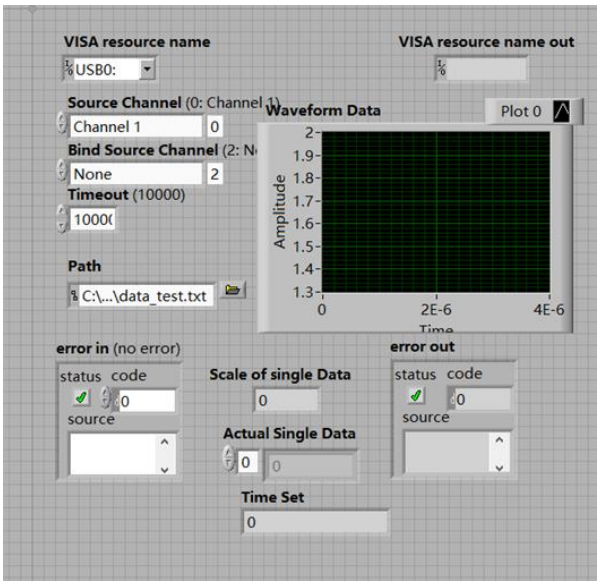

Figure 23. Front panel of the kernel VI for waveform saving

This kernel VI also returns the scale of the data collected each time, which is great feature for compiling.

Using this kernel as a sub VI, the whole data saving program is written, which enables us to save the waveform data for any assigned number of times.

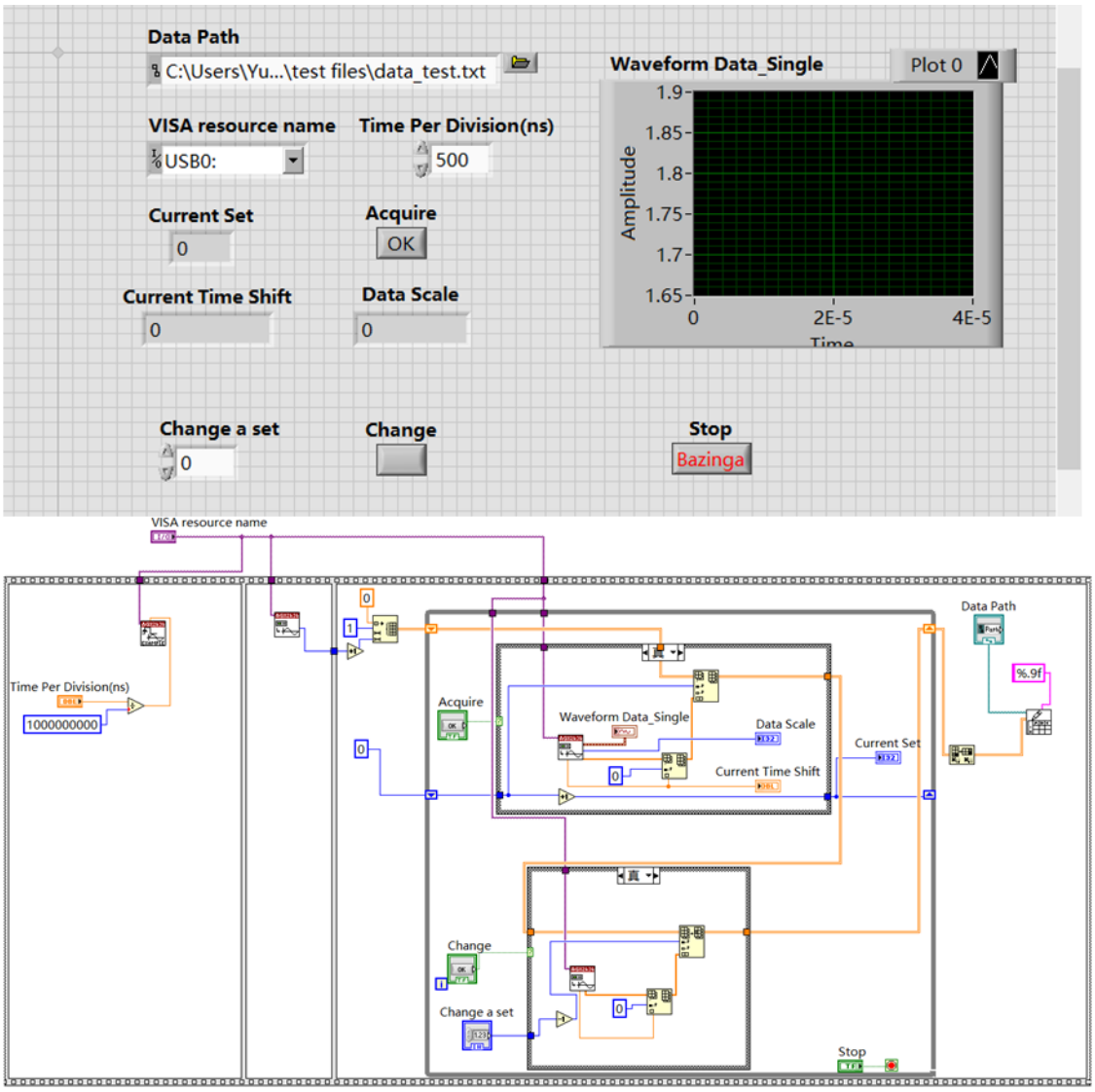

Figure 24. Front panel and the Block diagram of the waveform acquiring VI

This VI saves the waveform to the designated txt file. Each time when the ‘Acquire’ button is hit, the entire waveform displayed on the oscilloscope screen is saved as a row, and such row is displayed in the VI as well.

In addition, for each row, the time delay of each wave form is also recorded, saved as the first column in each row, which is a significant feature for later data process in each experiment.

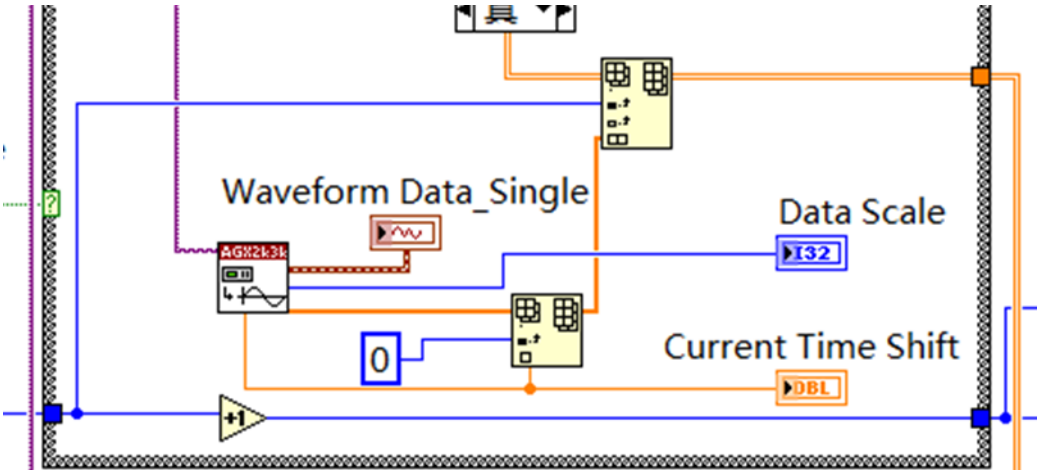

Figure 25. Saving the time delay of each wave form to the first column

Given these VI program written, it's considered to be feasible to integrate them all in one whole program.

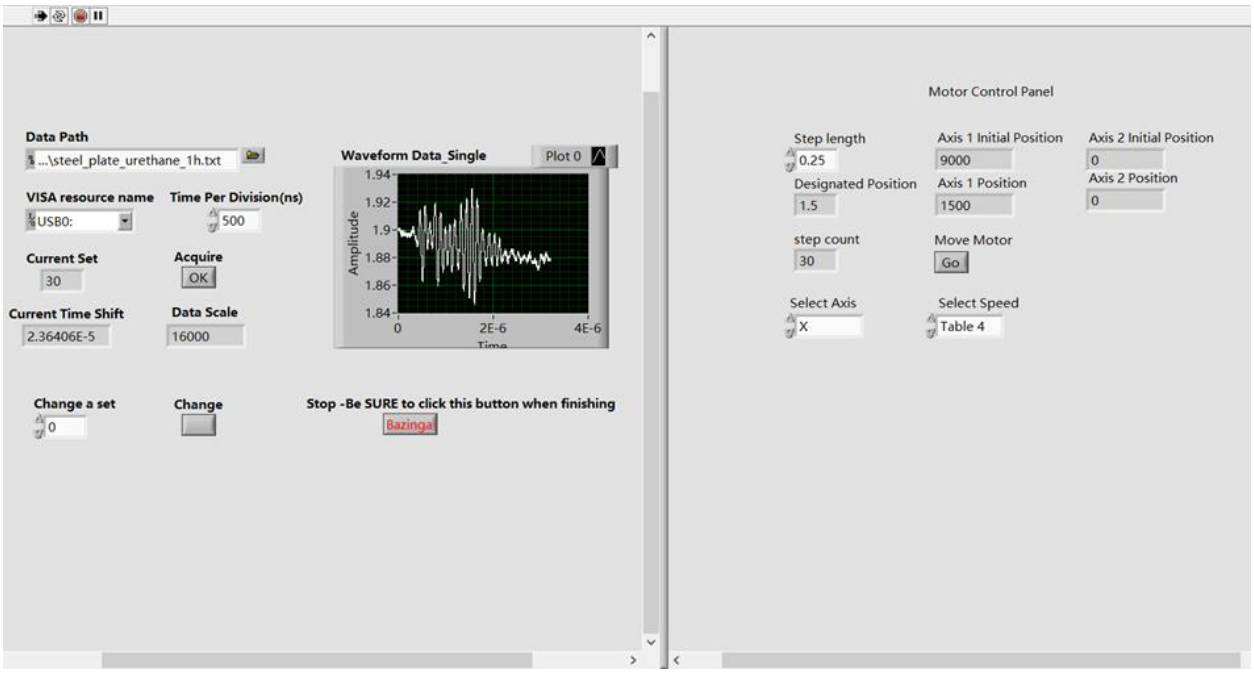

Figure 26. Front panel of the integrated VI for waveform saving and motor control

This integrated program allows the user to control and monitor the waveform and the motor operation at the same time, ultimately simplifying the working procedure of a test on the samples.

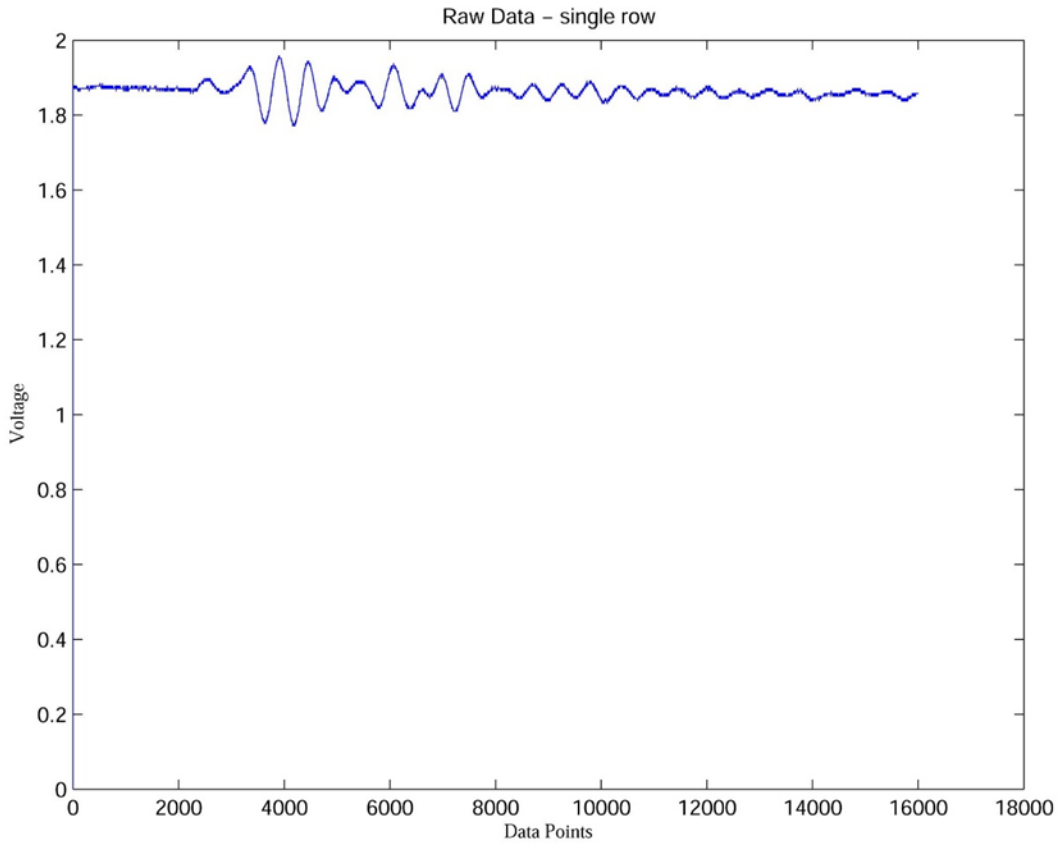

Figure 27. One single row of the raw data collected

Above is one single row of the raw data collected from an experiment. The data collected is typically 16000 points in length, due to the limitation of the memory of the oscilloscope. In time resolution, each point represents 0.2ns, hence each row of the raw data records the time span of 3.2μs of the waveform.

To be noticed, the first column of the data is near 0, as it records the time delay of the time form, typically to the order of 10^-5 seconds. This information is critical for the later data processing.

2.5 PULSER/RECEIVER OPERATION MODE

The model of the pulser/receiver used in the system is Olympus Model 5072PR, its panel and ports are shown as below.

Figure 28. Front and rear panel layout of the pulser/receiver

The pulse/receiver links to the transducer probe and the ociloscope in the following way, where a single transducer is adpated.

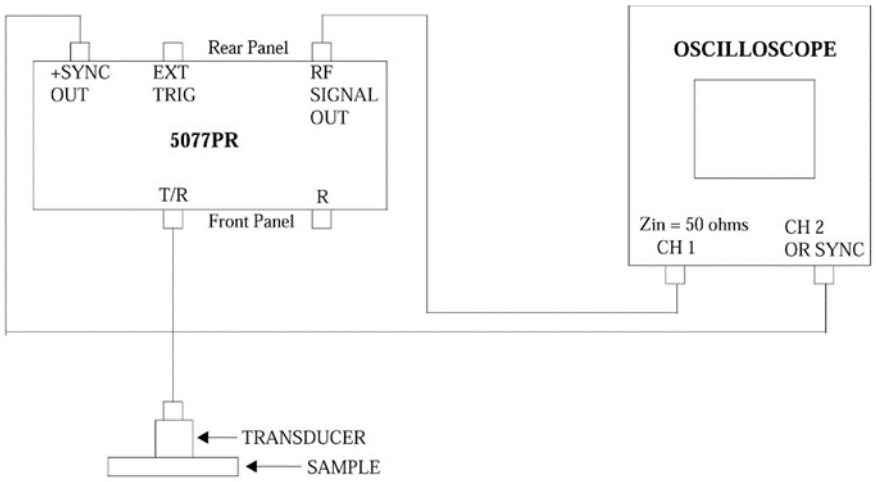

Figure 29. Cable connections for the pulse-echo operation (adapted from www.olympus-ims.com)

In actual practice, the RF (reference signal) is left blank, and the oscilloscope uses its own trigger signal.

2.6 FABRICATION OF THE TRANSDUCER PROBE

The PVDF transducer in this research is fabricated referring to the work from the group of D. Xiang et.al.

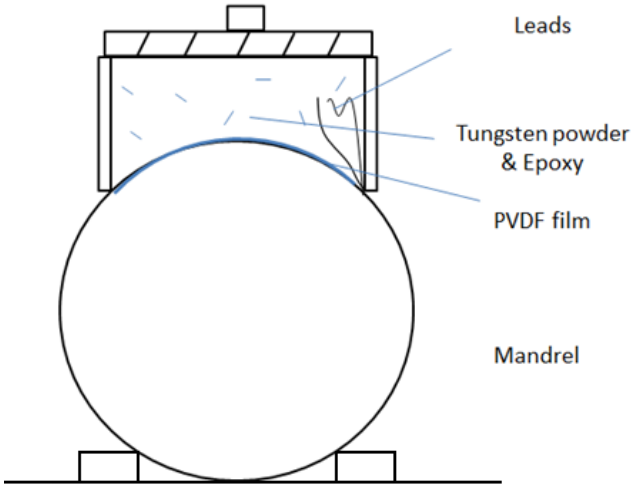

Figure 30. The method for fabricating the probe

A rectangular tube is sectioned according to the radius of the round tube, functioning as the frame. Different radius are chosen, of 1.5, 2 and 2.5 inch for comparison.

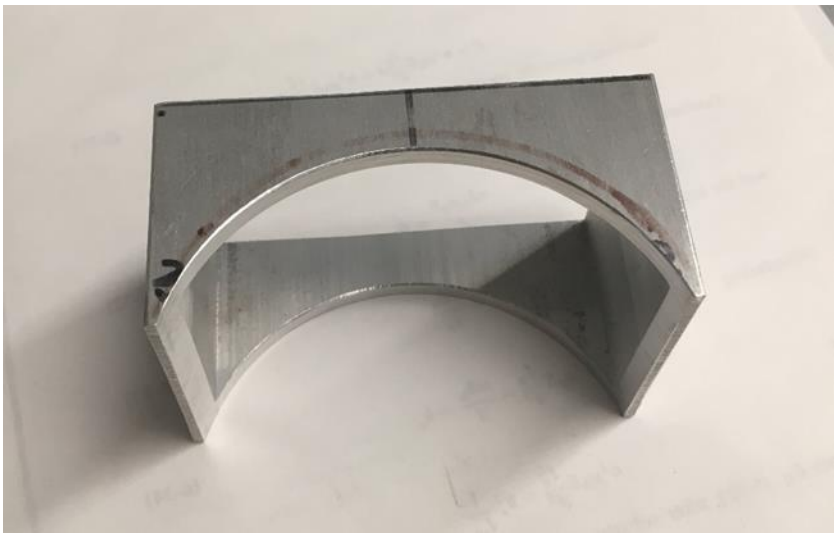

Figure 31. The transducer case sectioned from aluminum tube

Then we use tungsten powder mixed with epoxy gel as the backing material, with the weight ratio of 1:2. When the backing is solidified, the PVDF film is glued to the convex surface of the backing with a thin layer of epoxy.

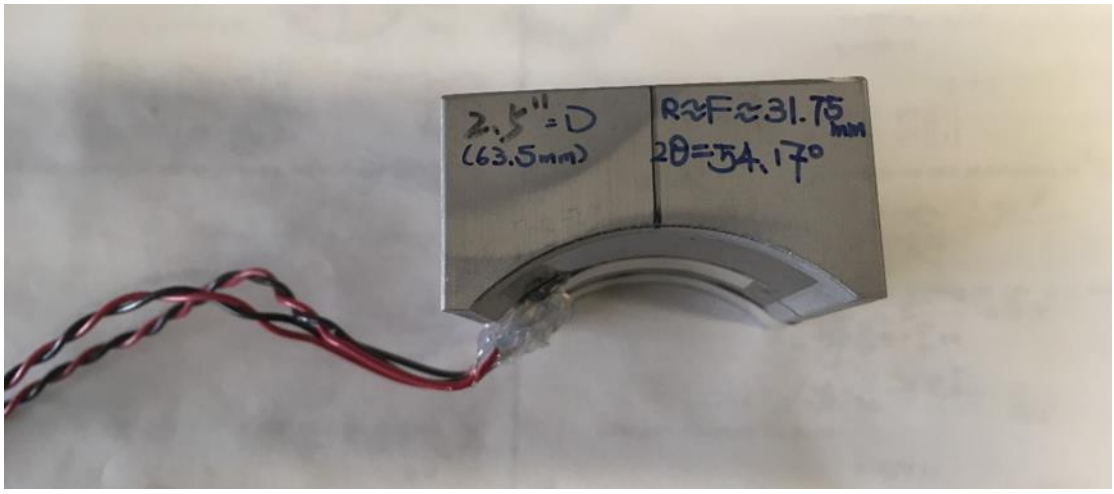

Figure 32. The transducer probe with PVDF film attached

Some threaded hole was drilled on the rear side of the probe, allowing us to fix it onto the motor stage:

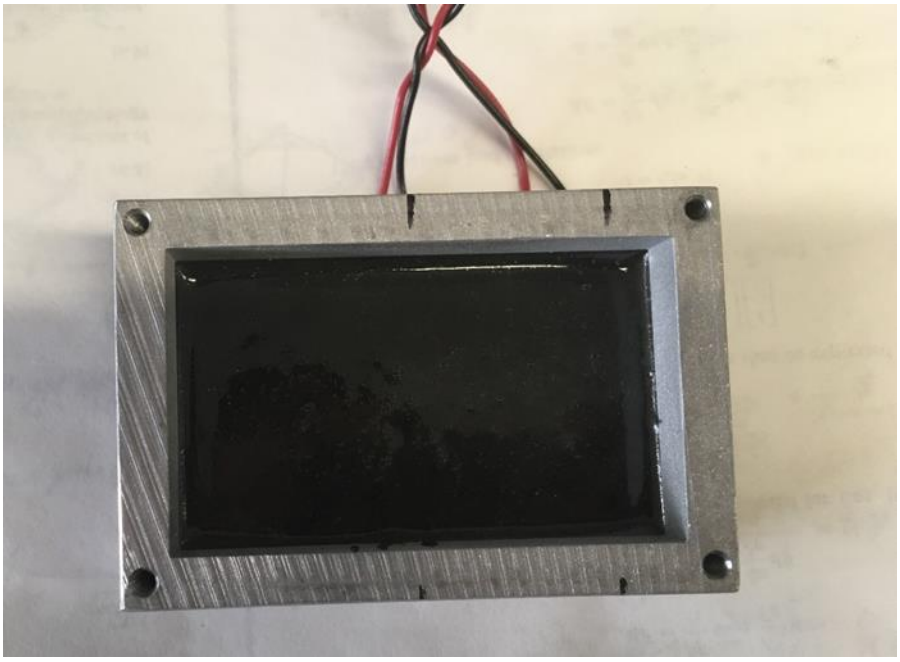

Figure 33. The threaded hole on the rear side of the probe

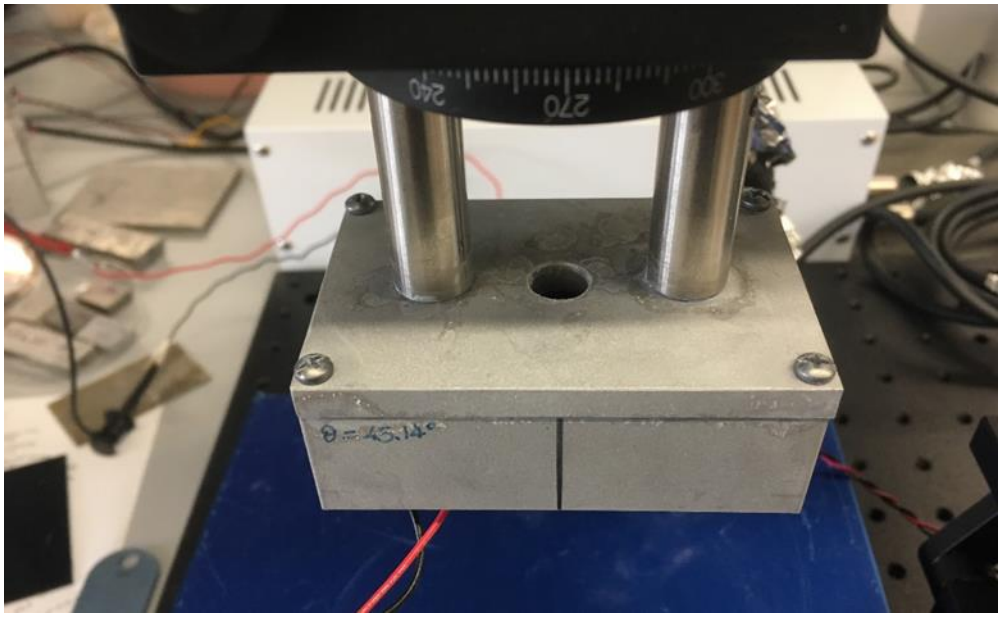

Figure 34. The way that the probe was fixed to the motor stage

The scale of the PVDF film we use is 1.3 inch ×0.5 inch:

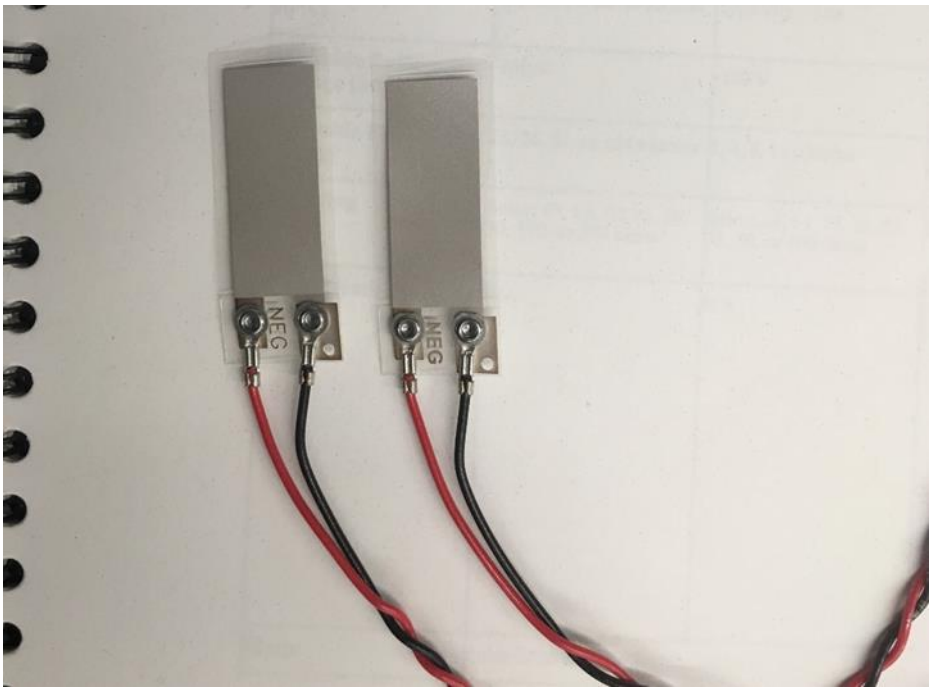

Figure 35. The PVDF film used in the system

The frequency response of the finished transducer is tested, shown in the figure below.

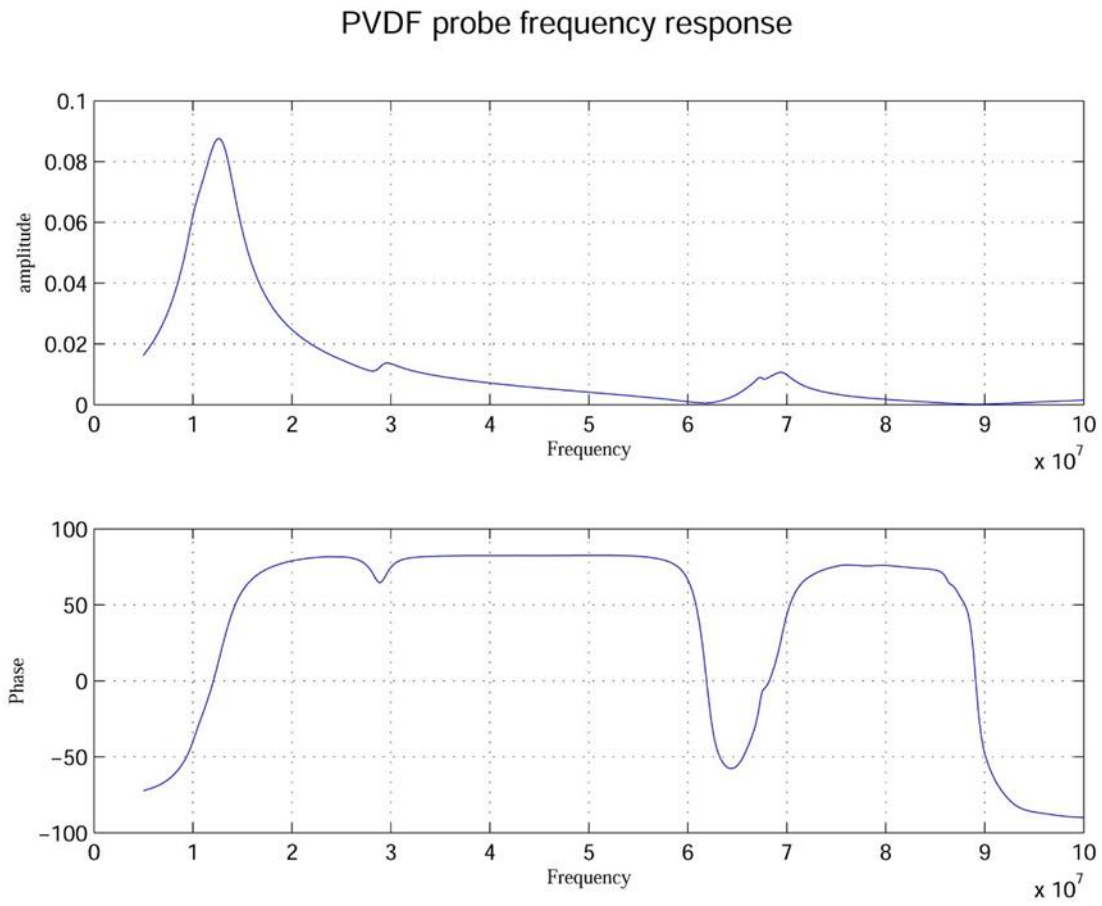

Figure 36. The frequency response of the PVDF transducer

The resonance peak appears around 13MHz, covering the frequency range of the sample waveforms.

3.0 TESTING ON THE COATING SAMPLES

3.1 THE SAMPLE METAL BASE

We chose standard 1/4 inch thick metal bar as the metal bar for the base to coat, including Stainless steel and Aluminum. For follow-on experiments, steel plate of 1mm thick is also used, as the typical material used in the car body shell.

3.2 PREPARATION OF THE SAMPLE

3.2.1 Prime layer

Self-etching primer coat is used to simulate the prime coat. The coat is prayed 3 times, waiting 10min between each spray. A solid prime layer is formed on the metal base after this step.

Figure 37. Spraying the prime coat

3.2.2 Color layer

Similar to the prime coat, the color coat is sprayed with same procedure, after the prime coating is completely finished.

Figure 38. Spraying the prime coat

3.2.3 Clear coat layer

There’re two types of the typical automotive coating materials in market. One is the thermosetting type, which would require the solidification at round 180 ℃ environment for hours, most of them consists of polyurethane. Such type is typically adapted in the original coat from the OEM assembly line.

The other type does not require high temperature curing, 80 ℃ or even room temperature would be enough for the curing process. The composition of this coating is typically Acrylic or

epoxy, and dual element polyurethane is also an option. Such type is more often used in after-market circumstance, a body shop for example.

Both type of the clear coats are prepared for the samples. We choose polyurethane for the case of high temperature curing, and Acrylic together with dual element polyurethane for room temperature curing.

The acoustic impedance of some clear coat material are listed below:

Table 3. The acoustic impedance of some clear coat materials

	c/[m/s]	ρ/[Kg/dm3]	Z_a/[MRayls]
Polyurethane	1700	1.04	1.80
Acrylic	2750	1.19	3.15
Epoxy	3070	1.25	3.84

3.2.4 Curing and drying

Similar to 3C1B procedure, the Polyurethane sample is baked at 180 Celsius for 2 hours in the electric oven, after spraying 4 to 5 times of the clear coat. The samples are then cooled to room temperature for the test.

Figure 39. Baking of the sample using electric oven

For the room temperature sample, we choose to cure it in normal temperature for 24 hours, until it's fully solidified.

3.2.5 Test procedure

The metal base of the samples are tested at first, as the comparison group of the coated samples.

For either type of coating, three samples are made simultaneously with the same procedure.

For the three Polyurethane coating samples that requires high temperature curing, the base metal is stainless steel. One sample is tested immediately after the final spray, one is tested after 1 hour baking and one after 2 hours baking.

For the three room temperature curing samples, we choose aluminum as metal base. One sample is tested immediately after the final spray, one is tested after 2 hours room temperature and one after 24 hours.

All the samples are tested from the focus distance at the beginning, increasing the defocus length at the step length of 0.25 or 0.1mm until reaching the size limit of the transducer probe.

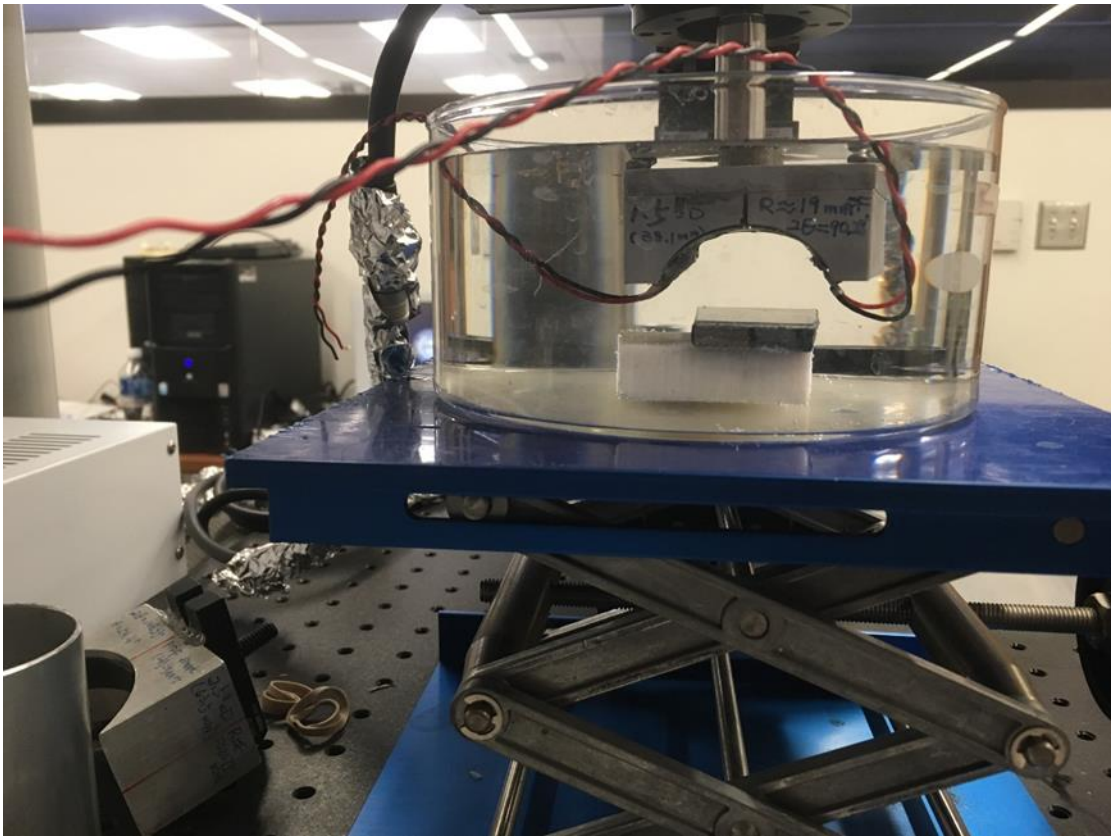

Figure 40. Positioning sample for one single test

4.0 DATE PROCESSING AND RESULTS

4.1 SIGNAL PROCESSING OF THE TESTING RESULT

4.1.1 Raw Data Processing

The typical raw data from one single test is shown below, which consists several rows of data at different defocus length:

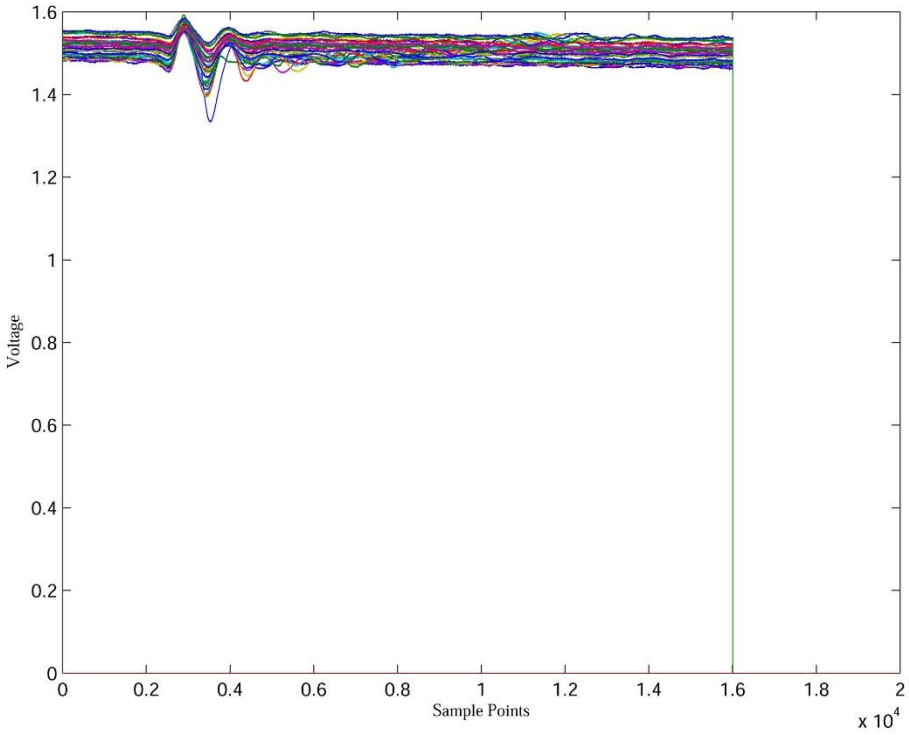

Figure 41. Raw data of waveform at different step distance

as the sample rate of the oscilloscope is 5GHz, the total 16000 sample points stands for 3.2μs of time period.

First we need to eliminate the ramp to minimize the error for the peak detection. To do this, the waveform of the transducer without any signal load is recorded, by linking the transducer directly to the pulser/receiver in air and record the waveform signal.

A total 25ms of the signal was recorded as follows:

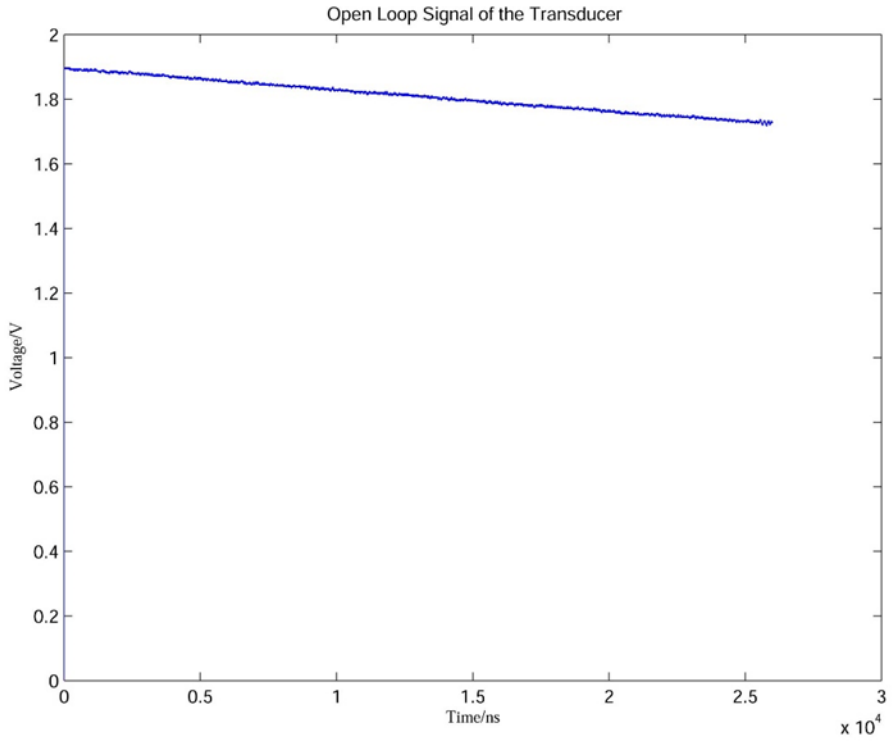

Figure 42. Open loop signal of the transducer

The first column of the signal is the time delay for the recorded signal, which is 1.4391×10^{-5} second. And for this 25ms long open loop signal, we can poly fit it as a function of time, in the form of exponential function.

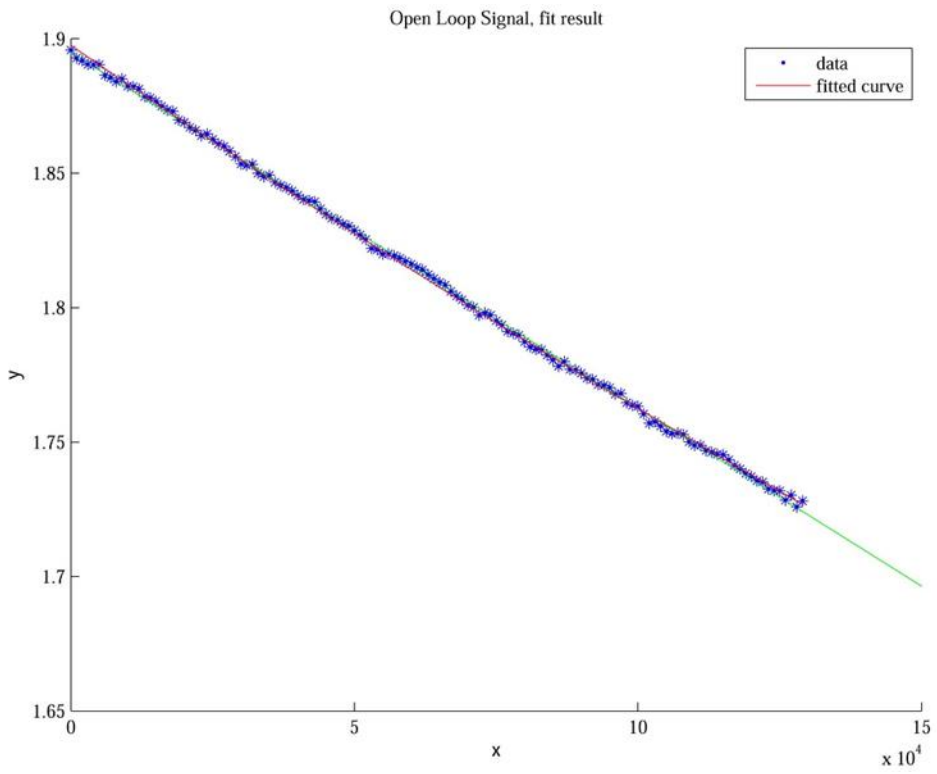

Figure 43. Signal Poly fit for the open loop signal of the transducer

In this way, we can substrate the open loop signal from the sample signal raw data, and align them to the same base voltage, which is shown in the figure below:

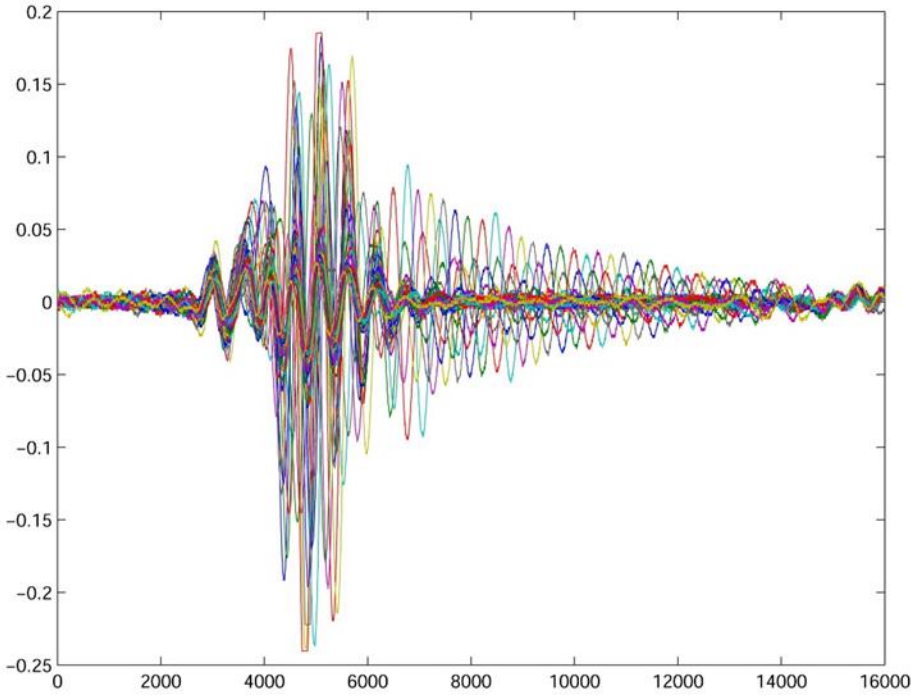

Figure 44. An example of raw data after voltage aligning

:

Considering the fact that during the test, each row may not be precisely aligned in time domain, we use the delay time information of each row:

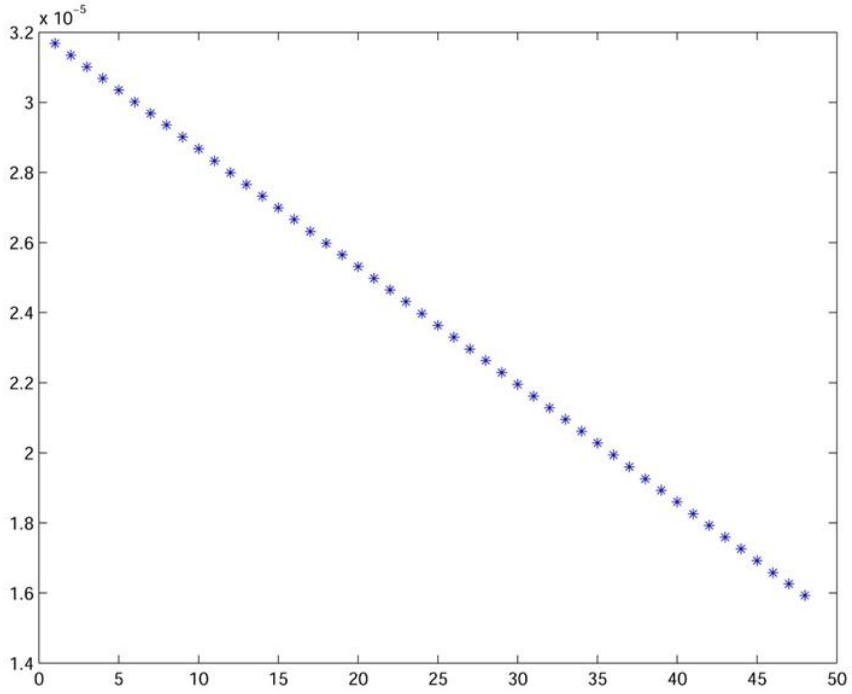

Figure 45. The time delay information of the raw data at different defocus position

and then differentiate it:

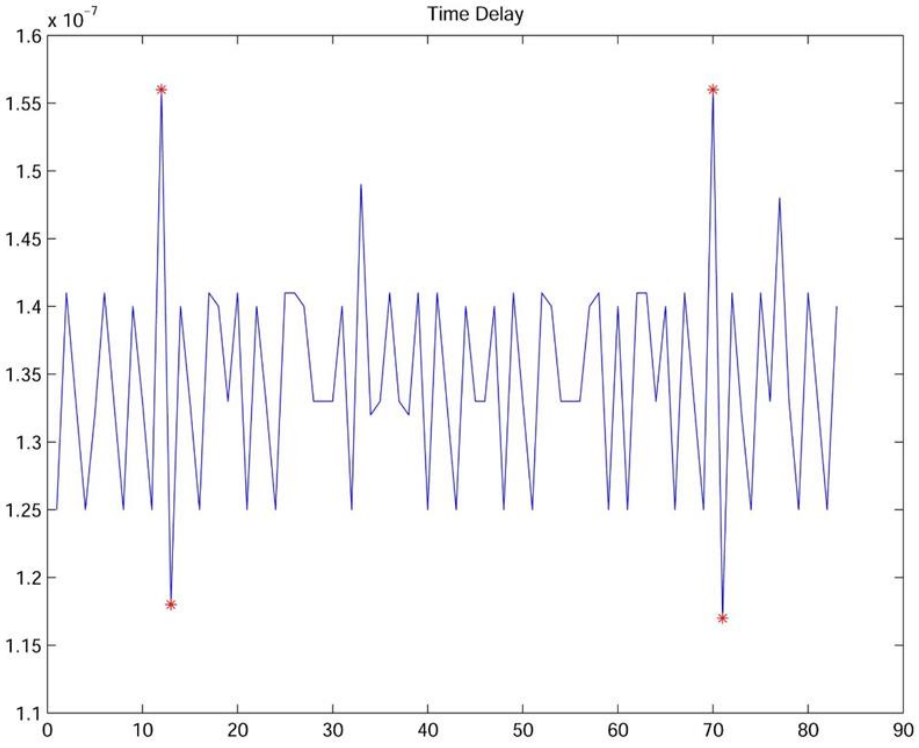

Figure 46. The time delay between each row

By abandoning the data with too much error, we use the rest data to calculate the average time delay, and use it as a reference to align each row in time domain:

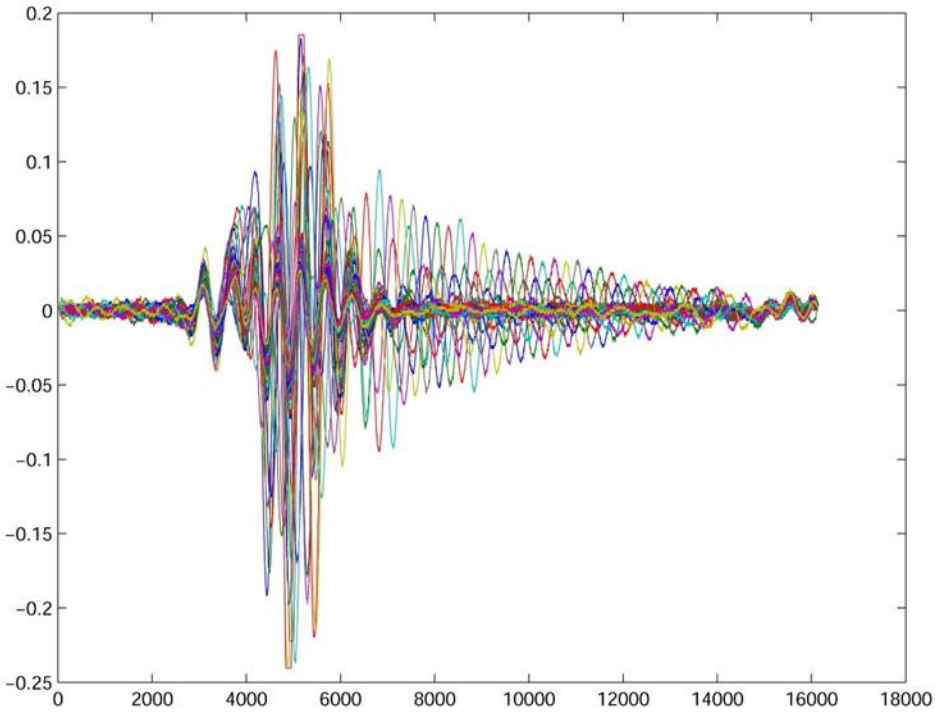

Figure 47. Data after time delay aligning

Giving each row an offset according to the row number, we can have an explicit view of the waveform data collected:

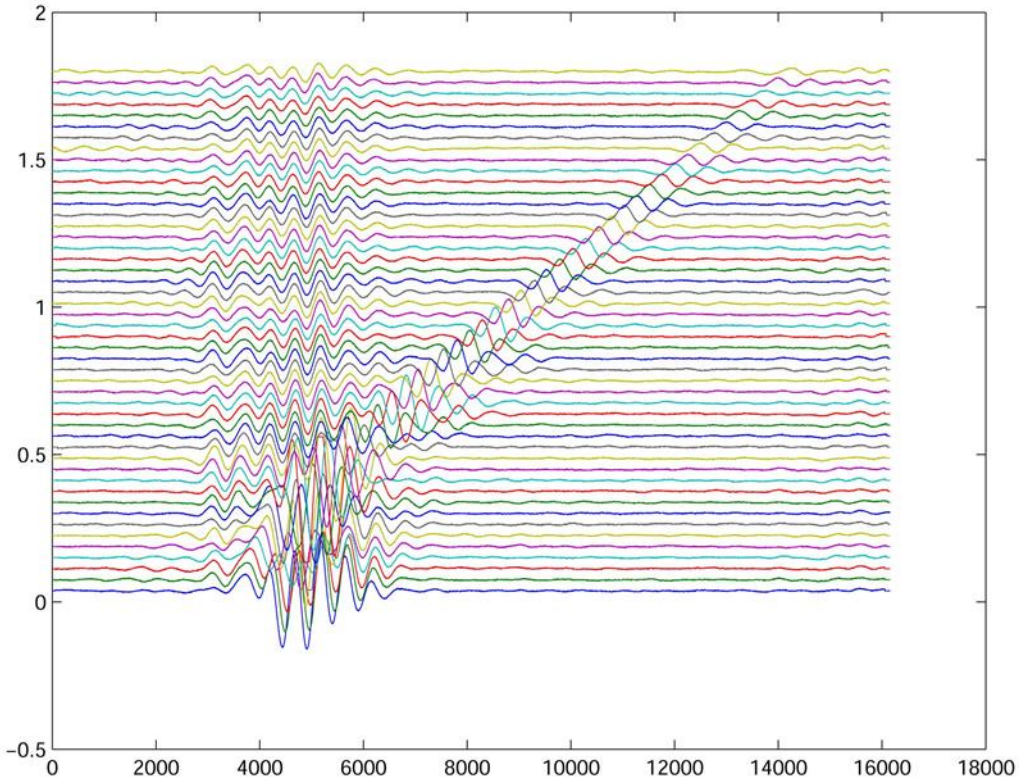

Figure 48. The data with offset, showing the leaky Rayleigh wave

4.1.2 Surface wave speed calculation

Till now, however, we cannot directly use the slope of the waveforms to calculate the surface wave speed, as the y value does not precisely correspond to the actual step distance between the sample and the transducer at each row.

At this time, the precise location where each peak of the surface wave of each row should be determined. Results of peak detection is shown below:

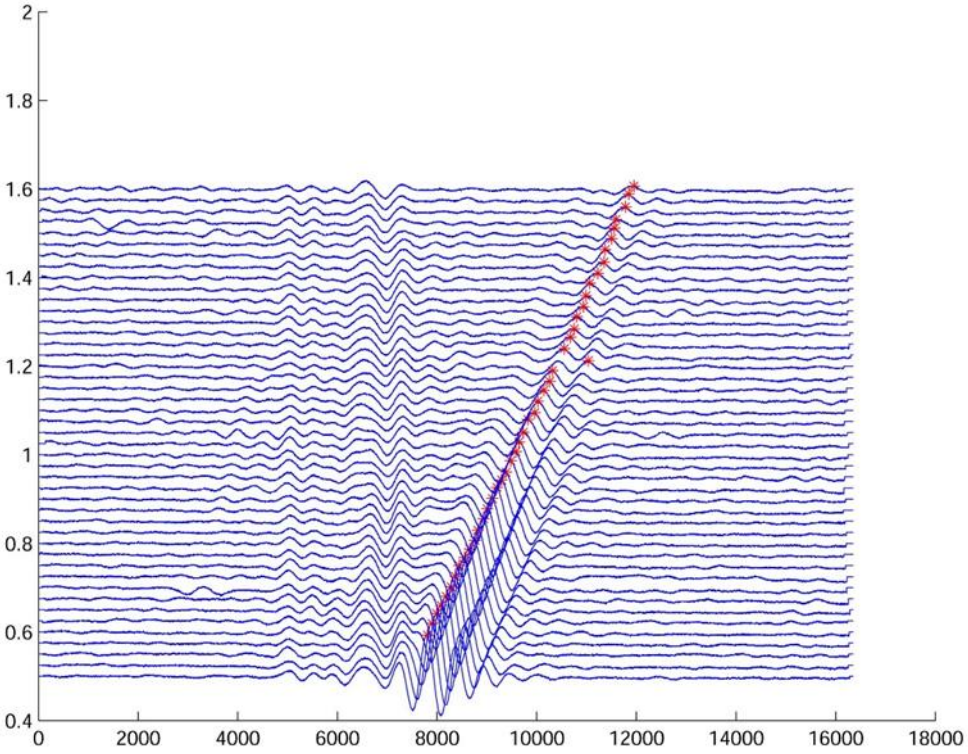

Figure 49. Results for peak detection of each row

Then use the x location of each peak as time information, which each point stands for 0.2ns, to draw the plot of the actual displacement of each row, i.e. the row number times the unit step distance:

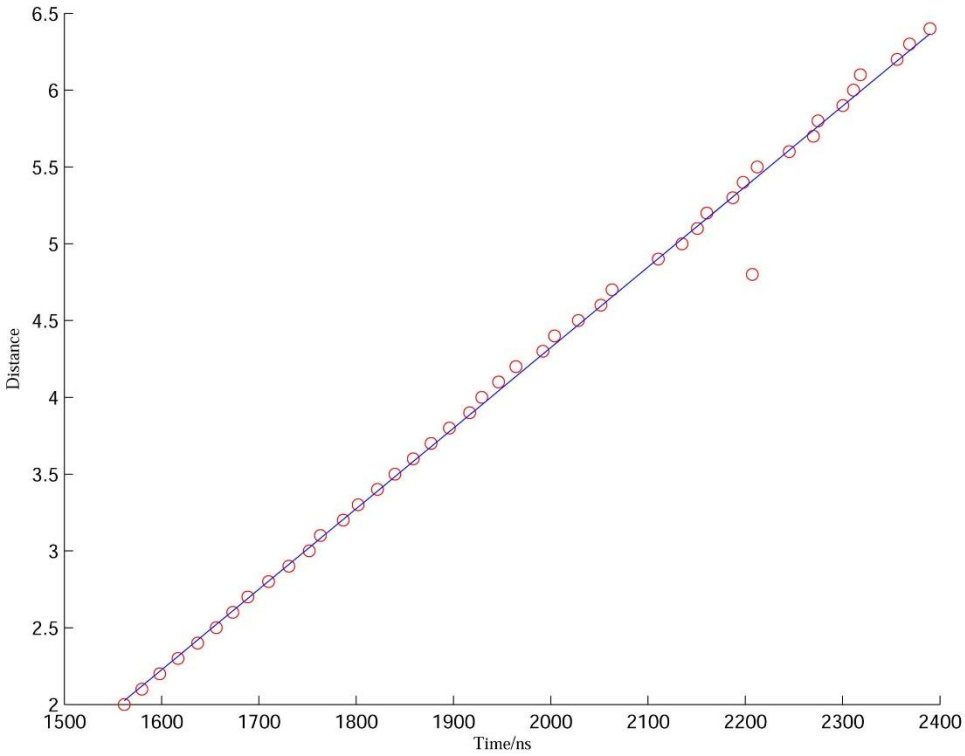

Figure 50. Distance as a function of travel time for surface wave

The slope of the curve fit, $\frac{dz}{dt}$ now could be used to calculate the surface wave speed, as mention before,

$$c_R = \left[\frac{1}{c_{Water}(\frac{dz}{dt})} - \frac{1}{4(\frac{dz}{dt})^2}\right]^{-1/2}$$

and the water sound speed in this experiment could be easily determined through various means, such as dividing the step length by the computed time delay between each rows.

And for example, for the stainless steel plate base, we now obtain that $\frac{dz}{dt}$ =5.0331, then we can calculate the surface wave speed to be 2.85 mm/μs. The results for the surface wave speed of all the base materials are listed as follows:

Table 4. Comparison of the experimental and reference surface wave speed of the metal materials

Material	Experimental/ $[mm/\mu s]$	Reference/ $[mm/\mu s]$	Impedance/ $[kg/(s \cdot m^2) \times 10^6]$
Aluminum	2.9090	2.906	17.10
Stainless Steel	2.8461	2.870	45.70
Steel(plate)	2.9695	2.945	47.28

4.1.3 Relations between coating and surface wave speed

The surface wave speed of the coated samples were tested and calculated for the reference, including stainless steel sample and aluminum.

Table 5. Surface wave speed of multiple coated samples (Reference data adapted from www.nde-ed.org.)

	Experimental/ $[mm/\mu s]$	Reference/ $[mm/\mu s]$
Aluminum	2.909	2.906
AL coated with Acrylic, 10min	2.9165	
AL coated with Acrylic, 2h	2.8846	
AL coated with Acrylic, 24h	2.8974	
Stainless Steel	2.8461	2.870
SLSteel with Polyurethane, 10 min	2.8449	
SLSteel with Polyurethane, 1h	2.8506	
SLSteel with Polyurethane, 2h	2.8212	

From the results above, we find that the coating layers does not influence the surface wave speed of the metal base, the deviation of the c_s results can be explained as system error of the experiments.

4.1.4 Relations between coating and surface wave intensity

We can also process the waveform data by looking at the amplitude of the surface wave at the corresponding positions.

If treating the coating layer as an interlayer for the surface wave to propagate through, we can recall the sound intensity transmission equation mentioned before:

$$t_I = \frac{I_t}{I_i} = \frac{4R_1R_3}{(R_1 + R_3)^2 \cos^2 k_2 D + (R_2 + \frac{R_1R_3}{R_2})^2 \sin^2 k_2 D}$$

The transmission factor as a function of the interlayer thickness is shown as below.

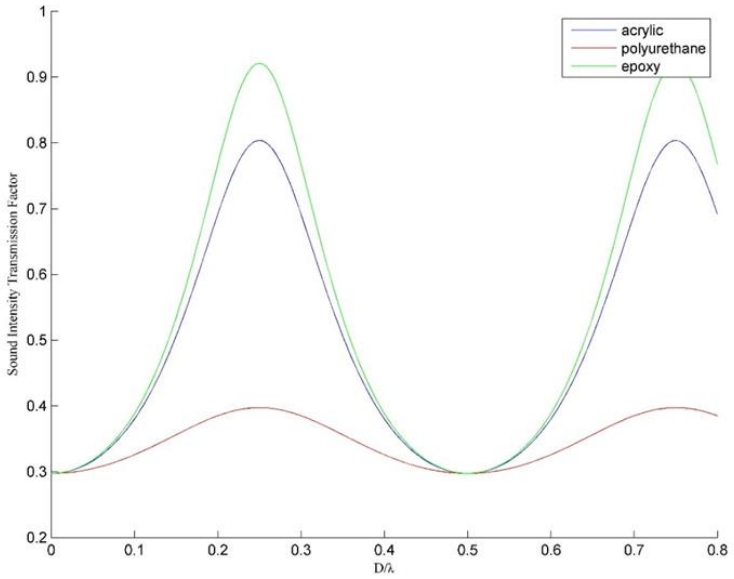

Figure 51. Sound intensity transmission factors of different material as a function of D/λ, aluminum base

Assuming the thickness of the coating is constant during curing, we can compute the intensity transmission factor as a function of the impedance of the interlayer.

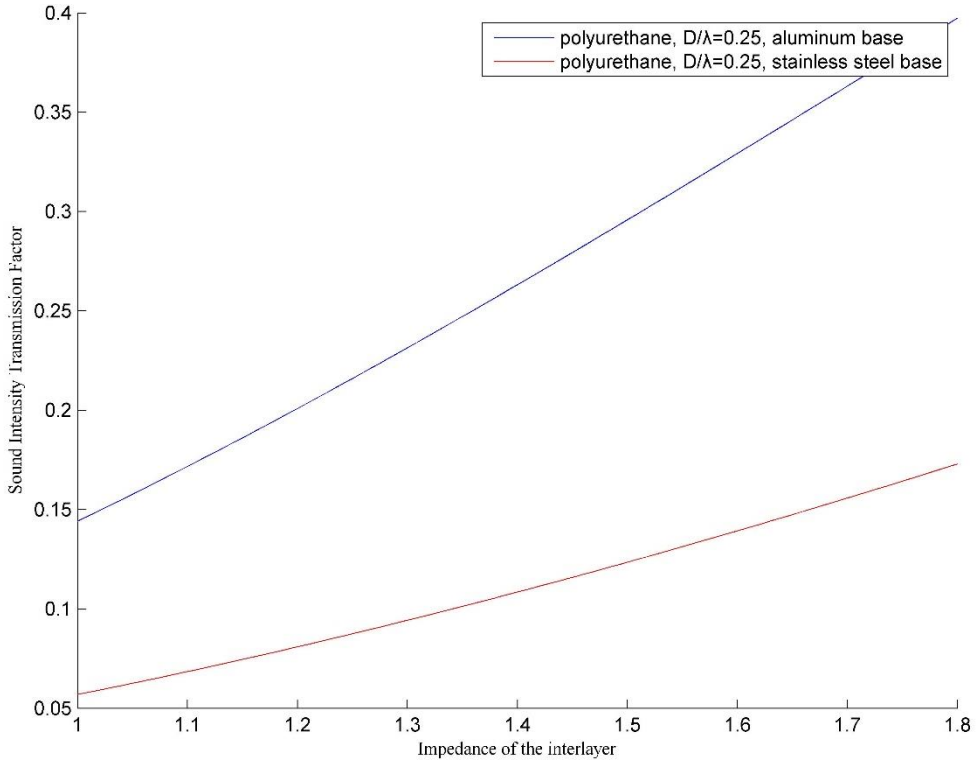

Figure 52. Intensity transmission factor as a function of the impedance of the interlayer

So in this case, the amplitude of the surface wave is computed for each row of the waveform signal:

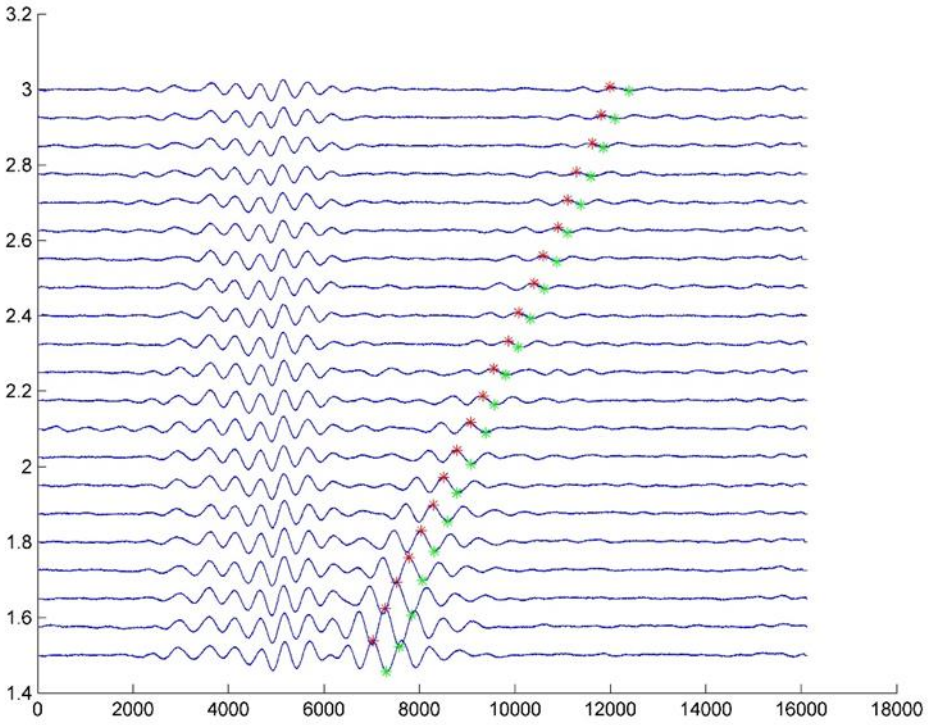

Figure 53. Peak to valley detection of the surface wave signals

Now we can compute the surface wave amplitude at different defocus position:

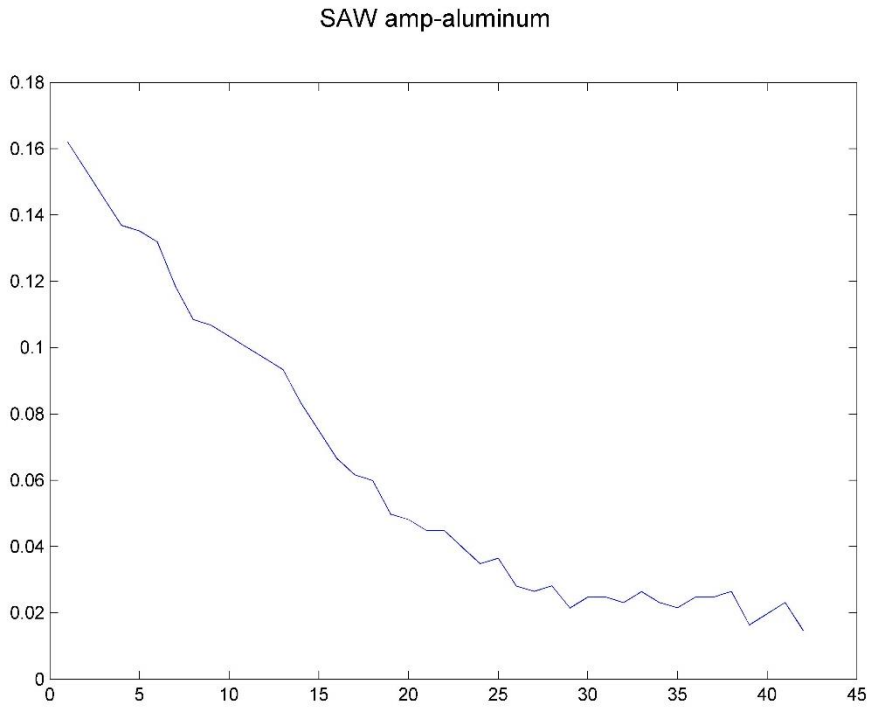

Figure 54. The surfave wave amplitude of aluminum as base metarial

Then we could also compute the surface wave amplitude of the coated samples, given the same defocus position:

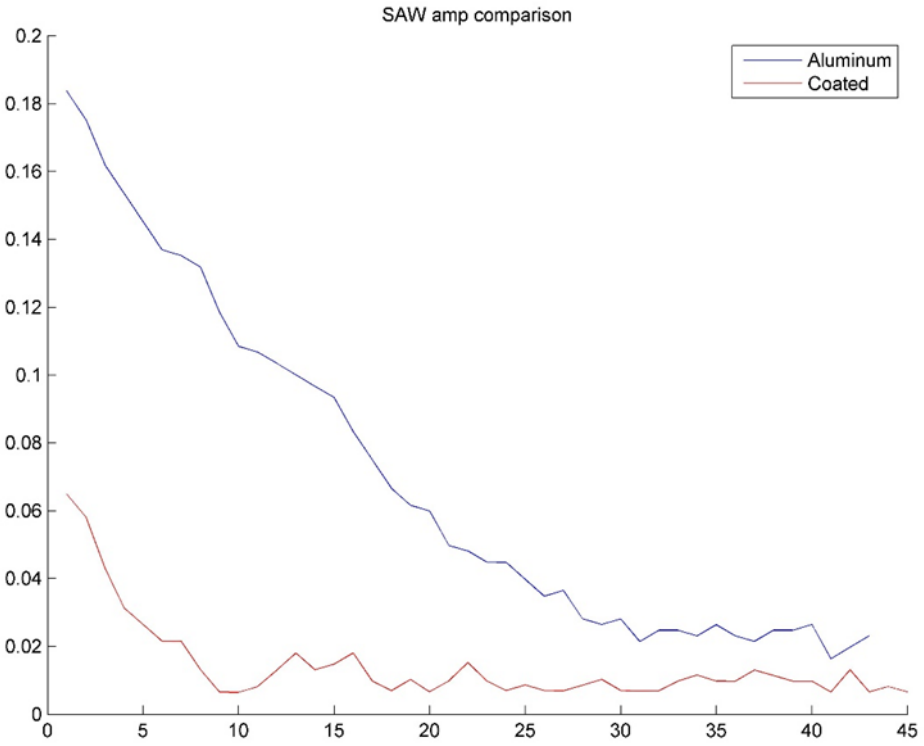

Figure 55. Surface wave amplitude comparison

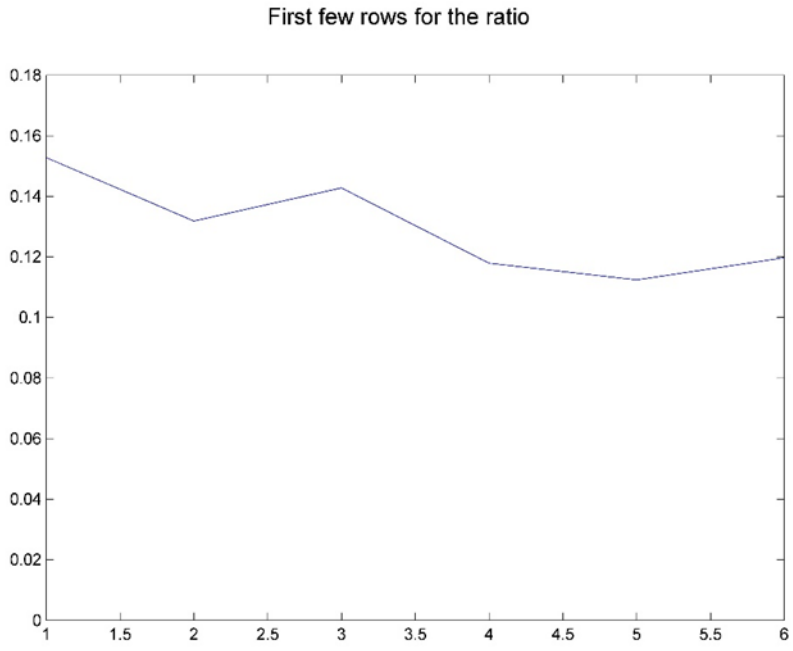

Figure 56. First 6 rows of the surface wave amplitude ratio

By calculating the ratio of the amplitude of the first few rows, we are now able to use intensity transmission factor to characterize the curing process (we set the metal base as the reference amplitude):

Table 6. The amplitude ratio of the surface wave of samples with different curing time

	Ratio
Aluminum Base	1
AL coated with Acrylic, 10min	0.267
AL coated with Acrylic, 2h	0.563
AL coated with Acrylic, 24h	0.597

A more precise experiment was performed with samples using aluminum base coated with dual element urethane, curing at room temperature and tested at various times:

Table 7. The amplitude ratio of the surface wave of samples with more collected curing time

	Ratio
Aluminum Base	1
AL coated with Urethane, 10min	0.152
AL coated with Urethane, 30min	0.307
AL coated with Urethane, 90min	0.323
AL coated with Urethane, 240min	0.355
AL coated with Urethane, 600min	0.362
AL coated with Urethane, 24h	0.356

As sound intensity is proportional to the square of the sound pressure, also, the stimulation signal from the transducer propagates twice though the interlayer when the surface wave signal is received, we can now compute the sound intensity transmission factor of the coating interlayer as a function of time:

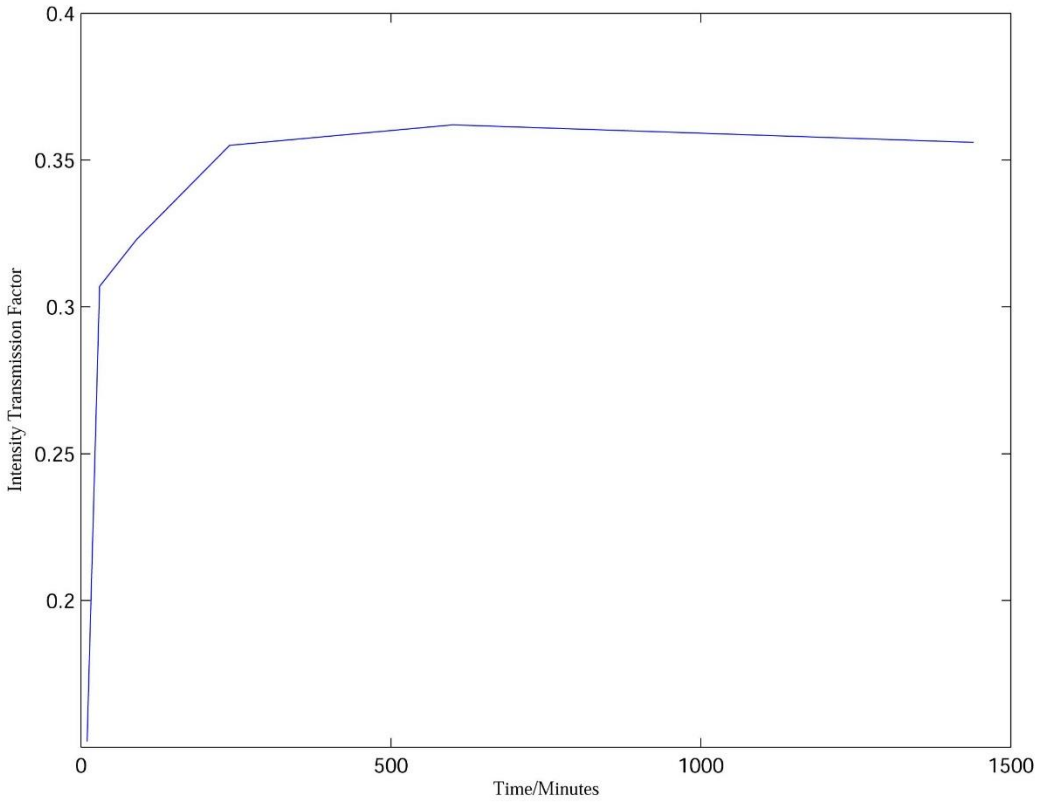

Figure 57. The Intensity Transmission Factor of the surface wave as a function of curing time

So now we are able to use intensity tansmission factor as a parameter to charactorize the curing process of the dual element polyurethane coat.

5.0 OTHER APPLICATION OF THE TESTING SYSTEM

5.1 CHANGE THE CONFIGURATION OF THE PROBE

5.1.1 Results using PVDF film with lower working frequency

If changing the transducer with PVDF film of lower working frequency, the results for the c_s agrees with the previous test

Table 8. Comparison of the surface wave speed calculated from different transducer experiments

	Experimental/$[mm/\mu s]$		Reference/$[mm/\mu s]$
	Lower Frequency	Higher Frequency	
Aluminum	2.909	2.892	2.906
Stainless Steel	2.842	2.827	2.870

5.1.2 Changing the probe of larger focusing length

The backing case of different focusing length (1.5, 2 and 2.5 inches) were manufactured in the first place, intending to receive the signal of the coating layer directly. However, due to the restrictions of the PVDF scale and property, no signal could be collected from the coating layer.

5.2 EVALUATION OF THE UNIFORMITY OF THE COATING LAYER

In this trail, one sample was specially made to simulate an uneven coating surface, by covering some part of the surface when adapting different sprays:

Figure 58. Unevenly coated sample

By adding a manual displacement stage, the testing system is now able to reveal the thickness distribution, by comparing the surface wave amplitude at multiple locations in 1 direction.

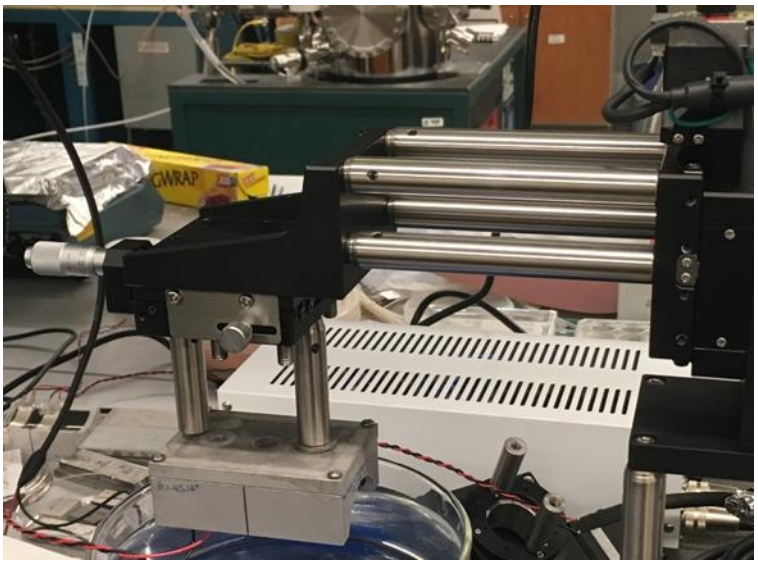

Figure 59. One dimension scanning configuration

In this experiment, 5 points are scanned, and the results are shown as below, using the amplitude of the aluminum surface wave as reference:

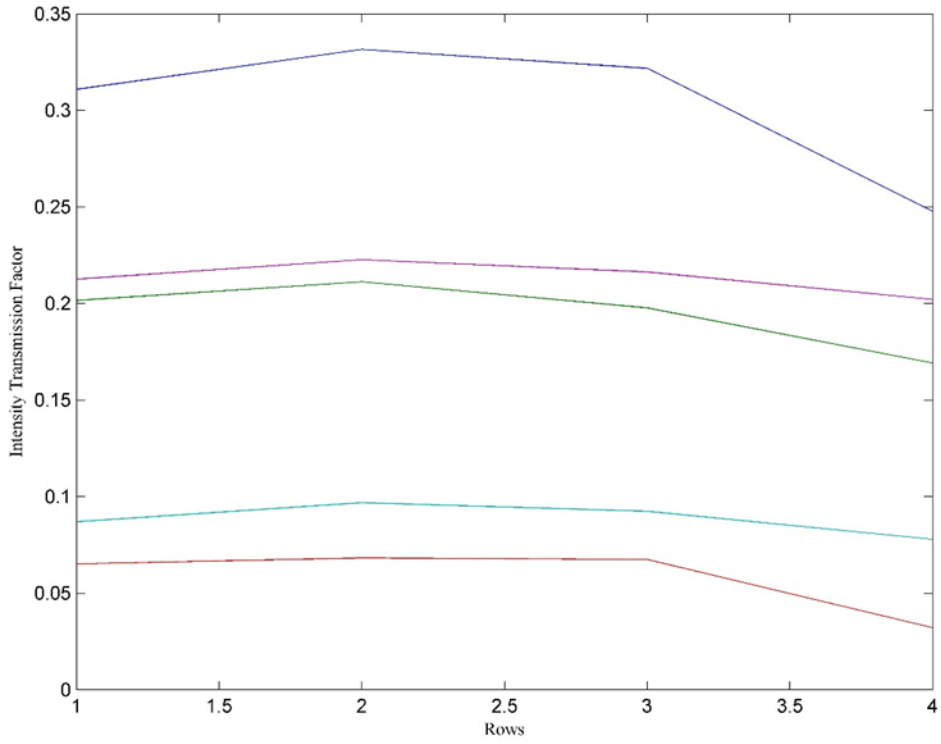

Figure 60. Intensity transmission factor of the surface wave of different sampling points

By computing the average of the first three rows, we are now able to plot the map of t_I regarding different points:

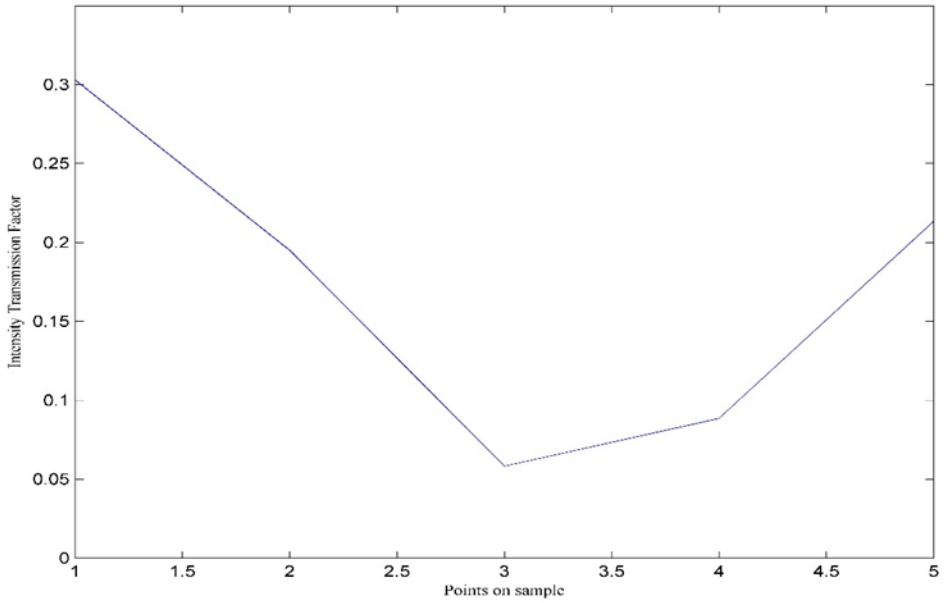

Figure 61. Distribution of intensity transmission factor of the surface wave on different points on the sample

6.0 CONCLUSIONS AND FUTURE APPLICATIONS

The line-focus transducer system provides an explicit view on the examination the mechanical properties of various materials, by studying the existing waveform of the surface wave. For the coated materials, some parameters are computed to quantify the curing process by measuring the properties of the surface wave from the coated metal.

However, if we're more interested in the coating layer alone, some improvement should be added to the test system along with the experiment protocols:

First, a transducer material with even higher working frequency is preferred to fit the target frequency span of the coating layers. Using ceramics SAW transducer might be a feasible approach.

Second, PVDF film with larger scale could be adapted for the line focus transducer probe, to cover greater angle range for the detection of the surface wave, as the critical angles (θ) of the surface wave of the coating materials are significantly larger than those of the metal base, thus the direct detection of the surface wave of the coating layer becomes not applicable for the current transducer set.

Third, directly examining the peeled coating layer could be a viable approach, using certain tools to peel off the entire coating. By this means, the influence from the metal base would be eliminated.

One large category of the samples in the designing of this research is the steel plate samples, to examine performance of the coated material using steel plate as the base. The results of the plate sample however, is too complicated to apply any surface wave methods. This may provide a great topic for future study.

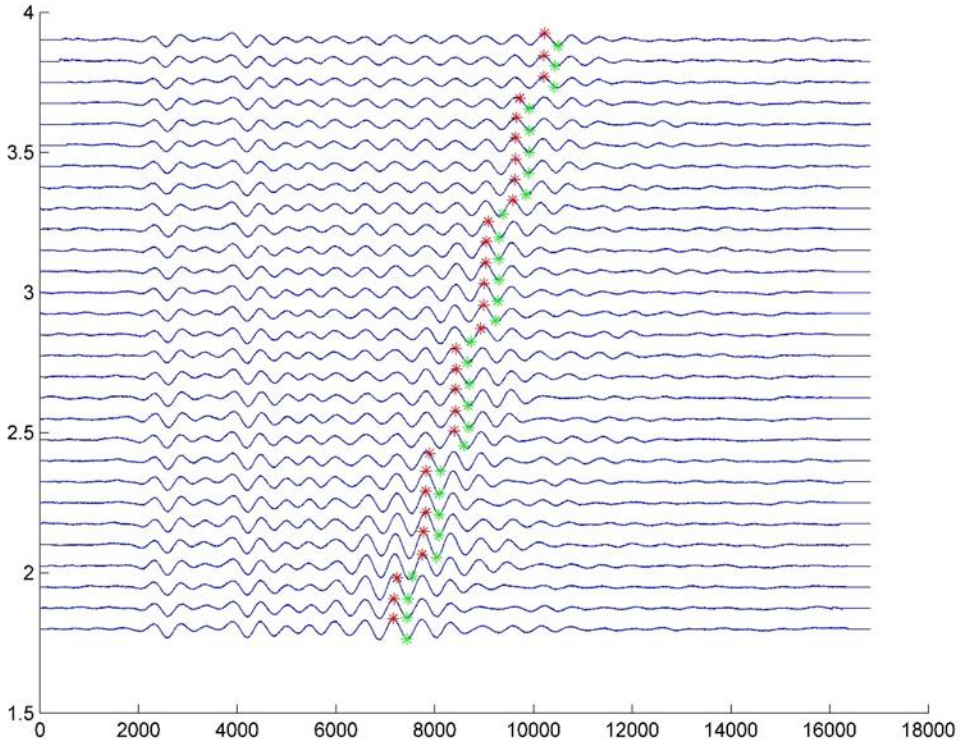

Figure 62. The waveform results of the coated steel plate

For the future application of this testing system, some new features could be added:

1) Real time data collection

Though the current control system has simplified the test procedure greatly, we could achieve an even better efficiency, if a real time data collection system (DAQ) is added. This requires high speed DAQ card like PCIe, which is available in multiple source.

2) Expanding the capacity of the motor stage

The stepper motor stage in the system is equipped with multiple control channels, thus provides multiple configuration options

By adding a rotation motor, the motor stage could be used for experiments on anisotropic materials.

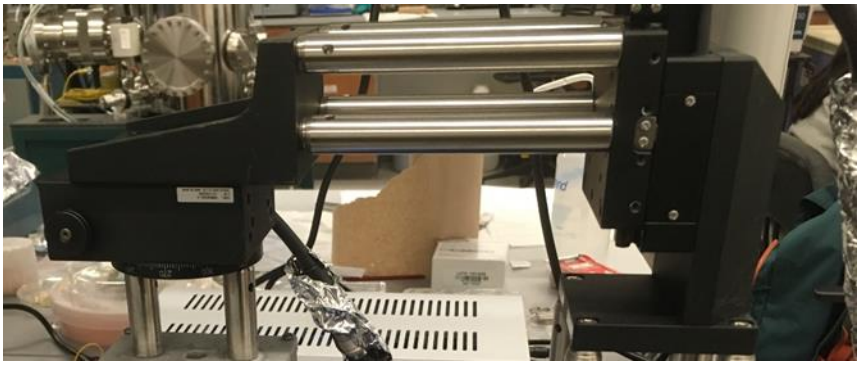

Figure 63. Rotation motor configuration

If a point focus transducer is adapted, and motor set is turned into a 3-axis stage using multiple channels from the controller, the system could be established for acoustic microscopy.

APPENDIX A

SURFACE WAVE EQUATION DERIVATIONS

A.1 THE DERIVATION OF THE SURFACE WAVE VELOCITY OF THE METAL MATERIAL

To discuss the surface wave equation in 2 dimensional case, where the free surface of ($x = 0$) of the solid, we let the solution of the wave equation to be in the form of :

$$\begin{cases} \phi = \phi_a e^{-\alpha x} e^{j(\omega t - k_s x)} \\ \psi = \psi_y = \psi_a e^{-\beta x} e^{j(\omega t - k_s x)} \end{cases}$$

Combining the motion equation:

$$\begin{cases} \rho \dfrac{\partial^2 \Phi}{\partial t^2} = (\lambda + 2\mu)\boldsymbol{\nabla^2}\Phi \\ \rho \dfrac{\partial^2 \psi}{\partial t^2} = \mu \boldsymbol{\nabla^2} \psi \end{cases}$$

Now we can derive:

$$\begin{cases} a^2 = {k_s}^2 - {k_L}^2 \\ \beta^2 = {k_s}^2 - {k_T}^2 \end{cases}$$

where $k_s = \frac{\omega}{c_s}$ is the wave number for the surface wave c_s. We can now set some new variables as:

$$\begin{cases} g^2 = (\dfrac{c_s}{c_T})^2 \\ q^2 = (\dfrac{c_T}{c_L})^2 = \dfrac{\mu}{\lambda + 2\mu} = \dfrac{1 - 2\sigma}{2(1 - 2\sigma)} \end{cases}$$

Then for α and β we have:

$$\begin{cases} \alpha = \dfrac{\omega}{c_s}\sqrt{1-qg} \\ \beta = \dfrac{\omega}{c_s}\sqrt{1-g} \end{cases}$$

For boundary condition, let the stress be 0 at the surface, as

$$\begin{cases} (T_{xx})_{(x=0)} = 0 \\ (T_{xz})_{(x=0)} = 0 \end{cases}$$

Combining the potential equation, we have:

$$\begin{cases} \omega^2[1-2(\dfrac{c_T}{c_s})^2]\phi_a + 2j\beta\omega\dfrac{{c_T}^2}{c_s}\psi_a = 0 \\ 2\omega\dfrac{\alpha}{c_s}\phi_a - j\left(\beta^2 + \dfrac{\omega^2}{{c_s}^2}\right)\psi_a = 0 \end{cases}$$

For a non-zero solution of ϕ_a and ψ_a, we have

$$\begin{vmatrix} \omega^2[1-2(\dfrac{c_T}{c_s})^2] & 2j\beta\omega\dfrac{{c_T}^2}{c_s} \\ 2\omega\dfrac{\alpha}{c_s} & -j\left(\beta^2 + \dfrac{\omega^2}{{c_s}^2}\right) \end{vmatrix} = 0$$

So finally the relations could be presented as:

$$\left[1-2(\frac{{c_T}^2}{{c_s}^2})^2\right]\left(\beta^2 + \frac{\omega^2}{{c_s}^2}\right) + 4\alpha\beta\left(\frac{c_T}{c_s}\right)^2 = 0$$

using the definition of g and q, the equation above could be written as:

$$g^3 - 8g^2 + 8(3-2q)g + 16(q-1) = 0$$

Through this relation we can calculate the surface wave velocity c_s, and determine the variables α and β from it.

The relation between surface wave speed and transverse wave speed is:

$$c_s = \sqrt{g}c_T$$

A.2 THE TRAJECTORY OF THE PARTICLES IN THE SURFACE WAVE

As the potential function of the surface wave consists of both ϕ and ψ, the surface wave could be treated as a combination of the both the longitudinal and transverse waves, thus the particle displacement is presented as:

$$\begin{cases} \xi = \frac{1}{j\omega}\left[\frac{\partial\phi}{\partial x} - \frac{\partial\psi}{\partial z}\right] \\ \zeta = \frac{1}{j\omega}\left[\frac{\partial\phi}{\partial z} + \frac{\partial\psi}{\partial x}\right] \end{cases}$$

where ξ stands for the displacement in x direction, ζ for displacement in z direction.

From the previous derivation, we have the solution in the following form:

$$\begin{cases} \xi = j\frac{\alpha\phi_a}{\omega}\left[e^{-\alpha x} - (\frac{\omega}{\alpha c_s})(j\frac{\psi_a}{\phi_a})e^{-\beta x}\right]e^{j(\omega t - k_s z)} \\ \zeta = \frac{\phi_a}{c_s}\left[e^{-\alpha x} - (\beta\frac{c_s}{\omega})(j\frac{\psi_a}{\phi_a})e^{-\beta x}\right]e^{j(\omega t - k_s z)} \end{cases}$$

and for ϕ_a and ψ_a,

$$j\frac{\psi_a}{\phi_a} = \frac{2a(\frac{\omega}{c_s})}{\beta^2 + (\frac{\omega}{c_s})^2}$$

thus,

$$\begin{cases} \xi = \frac{\alpha\phi_a}{\omega}\left[e^{-\alpha x} - \frac{2(\frac{\omega}{c_s})^2}{\beta^2 + (\frac{\omega}{c_s})^2}e^{-\beta x}\right]e^{j(\omega t - k_s z + \frac{\pi}{2})} \\ \zeta = \frac{\phi_a}{c_s}\left[e^{-\alpha x} - \frac{2\alpha\beta}{\beta^2 + (\frac{\omega}{c_s})^2}e^{-\beta x}\right]e^{j(\omega t - k_s z)} \end{cases}$$

writing in real form:

$$\begin{cases} \xi = A\cos(\omega t - k_s z + \frac{\pi}{2}) \\ \zeta = B\cos(\omega t - k_s z) \end{cases}$$

where

$$\begin{cases} A = \dfrac{\phi_a}{c_s}\left[e^{-\alpha x} - \dfrac{2(\frac{\omega}{c_s})^2}{\beta^2 + (\frac{\omega}{c_s})^2}e^{-\beta x}\right] \\ B = \dfrac{\alpha\phi_a}{\omega}\left[e^{-\alpha x} - \dfrac{2\alpha\beta}{\beta^2 + (\frac{\omega}{c_s})^2}e^{-\beta x}\right] \end{cases}$$

for the certain x value, i.e. the certain depth beneath the surface, A and B remains constant.

Thus, for ξ and ζ, with $\frac{\pi}{2}$ phase difference,

$$\frac{\xi^2}{A^2} + \frac{\zeta^2}{B^2} = 1$$

This explains that the trajectory of the particles in surface wave is an ellipse.

BIBLIOGRAPHY

[1] Norton, Michael Peter, and Denis G. Karczub. Fundamentals of noise and vibration analysis for engineers. Cambridge university press, 2003.

[2] Abraham, Ralph, Jerrold E. Marsden, and Tudor Ratiu. Manifolds, tensor analysis, and applications. Vol. 75. Springer Science & Business Media, 2012.

[3] [Online]. Available: http://www.geo.mtu.edu/.

[4] T. Ikeda, "Fundamentals of piezoelectricity," Oxford university press, 1996.

[5] H. Kawai, "The piezoelectricity of poly (vinylidene fluoride)," Japanese Journal of Applied Physics, vol. 8, no. 7, p. 975, 1969.

[6] Xiang, Dan, N. N. Hsu, and G. V. Blessing. "The design, construction and application of a large aperture lens-less line-focus PVDF transducer." Ultrasonics 34, no. 6 (1996): 641-647.

[7] Kawashima, Koichiro, Toshihiro Ito, and Kiichiro Mori. "Finite element simulation of leaky surface wave propagation excited by a line-focused transducer." In Review of Progress in Quantitative Nondestructive Evaluation, pp. 995-1002. Springer US, 1998.

[8] Bertoni, H. L., and T. Tamir. "Unified theory of Rayleigh-angle phenomena for acoustic beams at liquid-solid interfaces." Applied physics 2, no. 4 (1973): 157-172.

[9] Drafts, Bill. "Acoustic wave technology sensors." IEEE Transactions on Microwave Theory and Techniques 49, no. 4 (2001): 795-802. Harvard

[10] Ballantine Jr, David S., and Hank Wohltjen. "Surface acoustic wave devices for chemical analysis." Analytical Chemistry 61, no. 11 (1989): 704A-715A.

[11] Oralkan, Omer, A. Sanli Ergun, Jeremy A. Johnson, Mustafa Karaman, Utkan Demirci, Kambiz Kaviani, Thomas H. Lee, and Butrus T. Khuri-Yakub. "Capacitive micromachined ultrasonic transducers: Next-generation arrays for acoustic imaging?." IEEE transactions on ultrasonics, ferroelectrics, and frequency control 49, no. 11 (2002): 1596-1610.

[12] Sherrit, S., H. D. Wiederick, and B. K. Mukherjee. "Accurate equivalent circuits for unloaded piezoelectric resonators." In Ultrasonics Symposium, 1997. Proceedings., 1997 IEEE, vol. 2, pp. 931-935. IEEE, 1997.

[13] Lee, Yung-Chun, Jin O. Kim, and Jan D. Achenbach. "Measurement of stresses by line-focus acoustic microscopy." Ultrasonics 32, no. 5 (1994): 359-365.

[14] Yang, Che-Hua. "Characterization of piezoelectrics using line-focus transducer." In Review of Progress in Quantitative Nondestructive Evaluation, pp. 177-184. Springer US, 1998.

[15] Weglein, R. D., and R. G. Wilson. "Characteristic material signatures by acoustic microscopy." Electronics Letters 14 (1978): 352-354. Harvard

[16] Yamanouchi, Kazuhiko, and Kimio Shibayama. "Propagation and amplification of Rayleigh waves and piezoelectric leaky surface waves in LiNbO3." Journal of Applied Physics 43, no. 3 (1972): 856-862.

[17] Kushibiki, J., and N. Chubachi. "THEORETICAL ANALYSIS OF V (2) CURVES MEASURED BY ACOUSTIC LINE-FOCUS BEAM."

[18] Blanc, D., P. Laurent, J. Andrieu, and J. F. Gerard. "Convective and radiant (IR) curing of bulk and waterborne epoxy coatings as thin layers. Part I: Methodology." Polymer Engineering & Science 37, no. 12 (1997): 1959-1969. Harvard

[19] Véchot, L., I. Bombard, P. Laurent, and J. Lieto. "Experimental and modelling study of the radiative curing of a polyester-based coating." International Journal of Thermal Sciences 45, no. 1 (2006): 86-93.

[20] Decker, C., T. Nguyen Thi Viet, D. Decker, and E. Weber-Koehl. "UV-radiation curing of acrylate/epoxide systems." Polymer 42, no. 13 (2001): 5531-5541.

[21] Satyaprasad, A., S. K. Nema, N. K. Sinha, and Baldev Raj. "Deposition of thick and adherent Teflon-like coating on industrial scale stainless steel shell using pulsed dc and RF PECVD." Applied Surface Science 256, no. 13 (2010): 4334-4338.

[22] Lee, Yung-Chun, and Chi-Chen Chu. "A double-layered line-focusing PVDF transducer and V (z) measurement of surface acoustic wave." Japanese journal of applied physics 44, no. 3R (2005): 1462.

[23] Durand, Alain, Thierry Lalot, Maryvonne Brigodiot, and Ernest Maréchal. "Enzyme-mediated radical initiation of acrylamide polymerization: Main characteristics of molecular weight control." Polymer 42, no. 13 (2001): 5515-5521.

[24] Kushibiki, J-I., and Mototaka Arakawa. "A method for calibrating the line-focus-beam acoustic microscopy system." IEEE transactions on ultrasonics, ferroelectrics, and frequency control 45, no. 2 (1998): 421-430.

[25] Lee, Yung-Chun. "Line-focus acoustic microscopy for material evaluation." PhD diss., Northwestern University, 1994.